Seismic Oceanography in the Tyrrhenian Sea – Thermohaline Staircases, Eddies and Internal Waves

G.G. Buffett[1,2], G. Krahmann[2], D. Klaeschen[2*], K. Schroeder[3], V. Sallarès[4], C. Papenberg[2], C. Ranero[4], N. Zitellini[5]

[1]Institute of Earth Science - Jaume Almera (ICTJA), Spanish Superior Research Council (CSIC), Lluís Solé i Sabarís, s/n, Barcelona, E-08028, Spain

[2]GEOMAR Helmholtz-Centre for Ocean research Kiel, Wischhofstr. 1-3, Geb.8, 24148 Kiel, Germany.

[3]CNR – ISMAR, Institute for Marine Science, Arsenale - Tesa 104, Castello 2737/F, 30122 Venezia, Italy.

[4]Institute Marine Science (ICM), Spanish Superior Research Council (CSIC), Pg. Marítim de la Barceloneta 37-49, 08003, Barcelona, Spain.

[5]CNR – ISMAR, Institute for Marine Science - Bologna, Via Gobetti 101, 40129, Bologna, Italy.

[*]Corresponding author: Dirk Klaeschen (dklaeschen@geomar.de)

Key Points:

- For the first time, we are able to image the Northern Tyrrhenian Anticyclone to a depth of 800 m and to confirm the horizontal continuity of the extensive thermohaline staircases over lengths of more than 200 km.
- We calculate the internal wave field and find it to be anomalously weak in the center of the eddy and in the center of the staircases, while it is higher near the coastlines. Our results indicate that the most likely reason for this is because of the influence of the boundary currents.

Abstract

We use seismic oceanography to document and analyze oceanic thermohaline finestructure across the Tyrrhenian Sea. Multichannel seismic (MCS) reflection data were acquired during the MEDiterranean OCcidental survey in April-May 2010. We deployed along-track expendable bathythermograph probes simultaneous with MCS acquisition. At nearby locations we gathered conductivity-temperature-depth data. An autonomous glider survey added in-situ measurements of oceanic properties. The seismic reflectivity clearly delineates thermohaline finestructure in the upper 2,000 m of the water column, indicating the interfaces between Atlantic Water/Winter Intermediate Water, Levantine Intermediate Water, and Tyrrhenian Deep Water. We observe the Northern Tyrrhenian Anticyclone, a near-surface meso-scale eddy, plus laterally and vertically extensive thermohaline staircases. Using MCS we are able to fully image the anticyclone to a depth of 800 m and to confirm the horizontal continuity of the thermohaline staircases of more than 200 km. The staircases show the clearest step-like gradients in the center of the basin while they become more diffuse towards the periphery and bottom, where impedance gradients become too small to be detected by MCS. We quantify the internal wave field and find it to be weak in the region of the eddy and in the center of the staircases, while it is stronger near the coastlines. Our results indicate this is because of the influence of the boundary currents, which disrupt the formation of staircases by preventing diffusive convection. In the interior of the basin the staircases are clearer and the internal wave field weaker, suggesting that other mixing processes such as double-diffusion prevail.

1 Introduction

What are the mechanisms that are responsible for mixing in the ocean? Answering this question is currently one of the key tasks in ocean research because mixing of different water masses at the smallest scales helps drive global thermohaline circulation. Yet, the various mixing processes are not fully understood. One of the reasons for this is because the small-scale and short-lived water mass variations that partially mix are inherently difficult to determine; and usually a large number of observations is required to obtain representative numbers. In the last decade, a new technique called seismic oceanography (SO) was developed to image and investigate the properties of water masses using low frequency acoustic methods. This technique is based on multichannel seismic (MCS) reflection profiling, and it has been shown to be a powerful tool to study temperature (and less so, salinity) contrasts associated with oceanic fine-structure [Sallarès et al., 2009] in unprecedented horizontal resolution [e.g. Gonella and Michon, 1988; Holbrook et al., 2003; Biescas et al., 2008, Buffett et al., 2010, Dagnino et al. 2016].

In this paper we map, describe, analyze, and interpret the thermohaline fine structure of the Tyrrhenian Sea derived from an SO investigation that was carried out in April-May 2010 with the R/V Sarmiento de Gamboa and the R/V Urania. The goals of the survey were first, to map the water mass distributions and second, to try to gain insights into the mechanisms which drive mixing in the basin and at its periphery.

The study of the Tyrrhenian Sea offers a unique location to analyze a constrained set of mixing processes. This is because it is a confined sea with distinct water masses where the general circulation pattern is well-understood. It contains a large central volume of water with relatively static properties. The central basin is surrounded by a cyclonic boundary current with significantly different properties. Lateral exchange processes have been reported between the boundary currents and interior of the basin [Zodiatis and Gasparini, 1996]. At its center, it is isolated from strong lateral mixing effects. Under such conditions, and due to the particular vertical water mass distribution [Budillon et al., 2009], a particular kind of diapycnal mixing – double diffusion – occurs.

In this work we processed and interpreted nearly 1,000 km of MCS lines that were integrated with *in situ* oceanographic observations, including expendable bathythermographs (XBTs), conductivity-temperature-depth probes (CTDs), and for the first time in an SO survey, an

autonomous glider. This data set allows us to define the geometry of the dynamic eddies and the quasi-permanent thermohaline staircases in the Tyrrhenian Sea. We mapped the boundaries and interfaces between different water masses in fine vertical and horizontal resolution and we characterized the dynamics and mixing of water masses in key areas by quantifying the internal wave field based on the methods of Holbrook and Fer [2005] and Krahmann et al. [2008].

2 Oceanographic setting of the Tyrrhenian Sea

2.1 Origins and characteristics of the water masses and their circulations

The Tyrrhenian basin is a deep, semi-enclosed basin within the Mediterranean that was formed as a result of the Late Miocene-to-Present E-SE retreat of the Apennines-Calabrian subduction system leading to back-arc extension and magmatism in the Tyrrhenian basin [Prada et al., 2016]. It is bounded by Corsica, Sardinia, and Sicily to the west and south, and the Apennine peninsula to the east and north. The Tyrrhenian reaches a water depth of 3,600 m in the abyssal plains of Marsili and Vavilov and 3,400 m on the Cornaglia Terrace (Figure 1). The bathymetry of the basin restricts circulation to two main channels: the wide Sardinia channel between Sardinia and Sicily (max. depth 1,900 m); and the narrower, shallower Corsica Channel between Corsica and mainland Italy (maximum depth, 400 m). The smaller and shallower straits of Bonifacio and Messina do not contribute significantly to the large-scale circulation [Artale et al., 1994]. The circulation through the Sardinia channel is part of a complex exchange of water masses between the central basin of the Western Mediterranean (WMED), the Eastern Mediterranean (EMED), and the Tyrrhenian Sea.

The Corsica Channel is too shallow to permit the exchange of deep water masses (with a sill depth of about 400 m), forcing much of the generally cyclonic circulation to turn southward (Figure 1) along the Sardinia coast. During their circulation, the water masses entering the Tyrrhenian Sea mix with resident water masses.

The water masses of the Tyrrhenian Sea are commonly classified by their temperature and salinity characteristics and are mostly named after their place of origin, though they are significantly modified within the Tyrrhenian Sea and along their pathway to it. It is also important to note that the water masses are not separated by clear high-gradient boundaries but rather by up to several hundred-meter-thick boundary intervals. It is at these boundary

intervals between the cores of the different water masses where most seismic reflectors are found.

The uppermost water mass is Atlantic Water (AW), which is present from the surface to approximately 200 m depth (core depth 0–100 m). As the name suggests it originates as the surface inflow of Atlantic water into the Mediterranean through the Strait of Gibraltar [Millot, 1999; Viúdez et al., 1998]. Its hydrographic properties become modified by evaporation and by the entrainment of Mediterranean water during its path along the North African coastline [Millot, 1999]. The AW branches into two currents at the Sardinia Channel. One branch continues to the EMED basin through the Sicily Channel and the other enters the Tyrrhenian Sea where it joins the cyclonic circulation. Here the AW has low (for the Mediterranean) absolute salinities ($36.5 < S < 37.5$ g·kg^{-1}; throughout the manuscript we use absolute salinities) [Viúdez and Tintoré, 1995] with the lowest values in the southern part of the Sardinia Channel and then increasing along the large scale cyclonic flow. Its maximum salinity occurs at its westward outflow through the northern part of the Sardinia Channel. Its near surface temperatures vary substantially according to season. Below the mixed layer the AW temperatures are usually 14–15 °C [Millot, 1999].

Directly beneath the AW, but still within the 0–200 m depth layer, sometimes a colder — but still relatively very fresh — layer is found [Budillon et al., 2009], which forms a local temperature minimum. This Winter Intermediate Water (WIW) has been documented to form in the northwestern part of the WMED Sea and it might subsequently be advected into the Tyrrhenian Sea [Juza et al., 2013]; though some authors have hypothesized a local Tyrrhenian origin [Hopkins, 1988; Budillon et al., 2009].

The Levantine Intermediate Water (LIW) has the highest salinities in the Tyrrhenian Sea. It circulates approximately between 200 and 600 m depth (core depth 300–500 m). It is formed during winter in the eastern part of the EMED when dry, cold, and strong winds enhance mixing and evaporation leading to a vertical convection process [Sparnocchia et al., 1999]. The LIW then spreads out westward, and is funneled into the Western Mediterranean via the Sicily Channel [Sparnocchia et al., 1999], near the west coast of Sicily. Moving into the Tyrrhenian basin, it follows the north coast of Sicily and flows directly below the AW and WIW in the cyclonic circulation. In the Sicily Channel its salinities can reach about 38.8 g·kg^{-1} with maximum temperatures of 15 °C [Budillon et al., 2009]. Like the AW/WIW, the LIW's

lowest salinity maximum occurs at the end of its cyclonic circulation — in the northern part of the Sardinia Channel [Astraldi and Gasparini, 1994].

In the deepest part of the Sicily Channel another water mass of EMED origin finds its way into the Tyrrhenian Sea. The transitional Eastern Mediterranean Deep Water (tEMDW) forms in the deep area of the Sicily Channel between the Malta and Pantelleria troughs through a mixture of original Eastern Mediterranean Deep Water with the LIW [Bonanno et al., 2014]. The tEMDW is characterized by somewhat lower salinities and temperatures than the LIW but it is still warmer and saltier than the Western Mediterranean Deep Water (WMDW). Both the tEMDW and the LIW have varying water mass properties [e.g. Cardin et al., 2015]. Directly after passing the Sicily Channel, tEMDW cascades down the north slope of Sicily, where it mixes with the resident Tyrrhenian Sea water and settles at depths between 1,000 and 1,850 m [Sparnocchia et al., 1999]. This water is usually included within the fairly broad range of waters called Tyrrhenian Deep Water (TDW).

Below these two water masses of EMED origin observations suggest that, especially at levels below 1,500 m, WMDW also enters the Tyrrhenian Sea [Millot, 1999; Rhein et al., 1999] and mixes with the resident water masses. While older observations [Millot, 1999] indicated that the resulting water mass filled the deeper parts of the basin as Tyrrhenian Deep Water (TDW), more recent observations show strong variations in the water mass properties below 1,500 m implying either a change in the source water masses, their mixing ratios, or a different formation process altogether [Fuda et al., 2002].

In summary, four water masses are thus usually distinguished in the Tyrrhenian Sea: basin-wide one finds AW as the uppermost fresh water mass at depths from 0–200 m; WIW is sometimes found underneath the AW as a fresh and cold water mass but still within the upper 200 m; LIW is the saltiest water mass in the basin covering the range from about 200–700 m with the highest salinities at the core depth of about 400–500 m; finally the TDW describes a very wide range of fresher and colder waters below 700 m with a core depth deeper than 1,500 m.

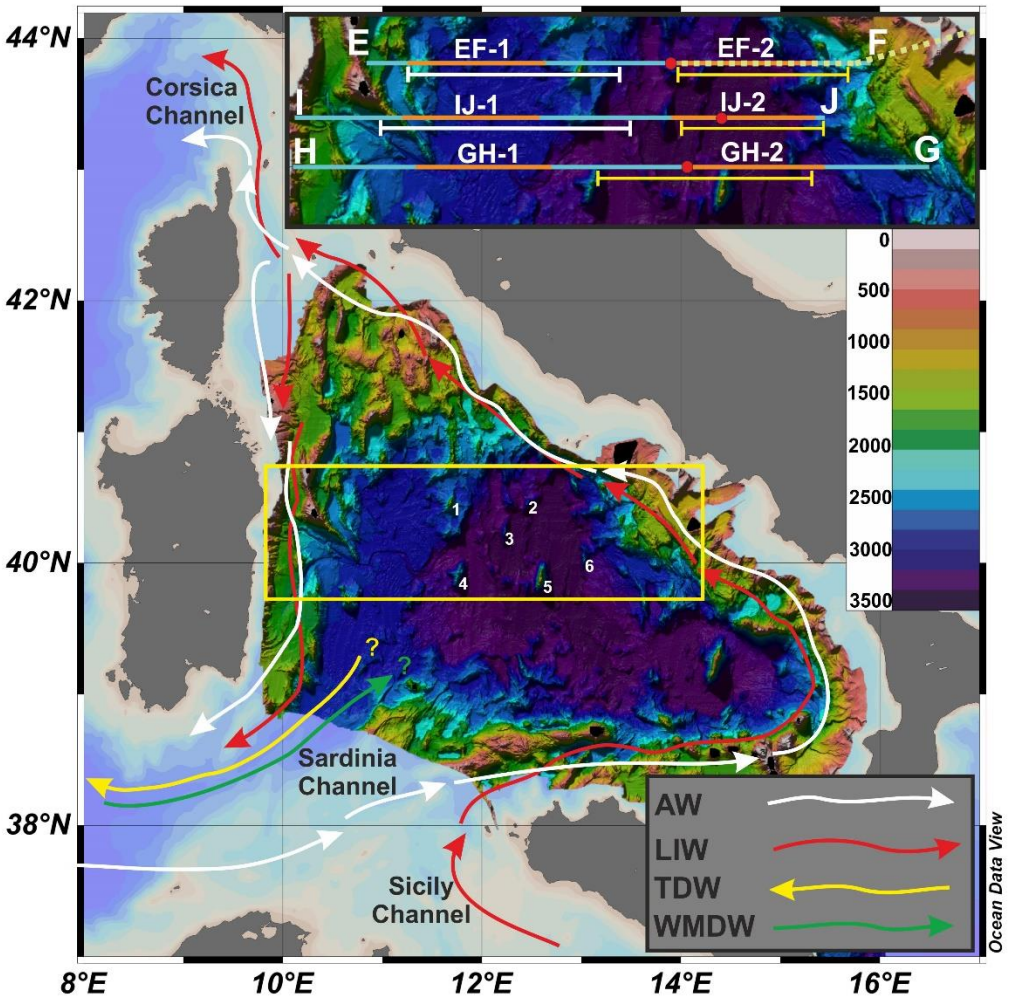

Figure 1 - Circulation in the Tyrrhenian Sea (modified after Millot [1999]) superimposed on multibeam bathymetry (MediMap Group [2005]) — depth color scale given in meters at right. Path of Atlantic Water (AW) shown in white; Levantine Intermediate Water (LIW) shown in red; Tyrrhenian Dense Water (TDW) shown in yellow; Western Mediterranean Deep Water (WMDW) shown in green. Selected seafloor features are 1: Secchi Seamount; 2: Farfalla Seamount; 3: Caesar Seamount; 4: Magnaghi Volcano; 5: Vavilov Seamount; 6: Flavio Gioia Seamount, [Mariani et al., 2004]. *Inset*: locations of seismic sections are shown in light blue; XBT deployment segments are indicated in orange; autonomous glider deployment shown in dotted yellow; eddy-dominated locations (Figure 3) are indicated by white segments; staircase-dominated regions (Figures 4, 5 and 6) are indicated by yellow segments; CTD locations are shown as red circles.

2.2 Meso-scale eddies

Surface eddies are a regular feature in the Tyrrhenian Sea albeit at a much weaker level than in the rest of the Western Mediterranean Sea [Poulain et al., 2012]. Some of these eddies are thought to translate from the Algero-Provençal basin, entering the Tyrrhenian through the wide Sardinia–Sicily Channel [Bouzinac et al., 1999]. This is probably aided by the flow of the AW into the basin. Budillon et al. [2009] surveyed the Tyrrhenian Sea using CTD measurements supplemented with satellite altimetry data, also finding meso-scale eddies. Rinaldi et al. [2010] reported an eddy pair for the northwestern part of the Tyrrhenian Sea. Driven by the typically westerly winds coming through the Strait of Bonifacio, these eddies are quasi-persistent [Artale et al., 1994]. The northern eddy rotates in an anti-clockwise direction and is known as the North Tyrrhenian Cyclone (NTC), while the southern one rotates in a clockwise direction and is known as North Tyrrhenian Anticyclone (NTA). Apart from these surface eddies the Tyrrhenian Sea hosts subsurface eddies which are not easily detectable at the sea surface. These are typically formed by the intermediate water masses WIW and LIW and are also known as mode-water eddies [Testor et al., 2005; Budillon et al., 2009].

Eddies play an important role in mixing the different physical, chemical, and biological properties of water masses. They are therefore important to global ocean circulation. Eddies have been imaged and analyzed with seismic oceanography many times (e.g. Holbrook et al. [2003]; Biescas et al. [2008]; Buffett et al. [2009]; Klaeschen et al. [2009]; Buffett et al. [2010]; Quentel et al. [2010]; Ménesguen et al. [2012]; Barbosa Aguiar et al. [2015]) but they have never before been seismically imaged in the Mediterranean Sea.

2.3. Thermohaline staircases

Thermohaline staircases in the Tyrrhenian Sea have long been reported for the depth interval of 500–2500 m [e.g., Tait and Howe, 1971; Johannessen and Lee, 1974]. Certain combinations of the vertical stratification of heat and salt allow for particular exchange processes between the water masses [Ruddick and Gargett, 2003]. Driven by the different molecular diffusivities of heat and salt, the diapycnal exchange is locally enhanced and gives rise to the thermohaline staircases. In the Tyrrhenian Sea, the most ubiquitous form of double-diffusion (salt-fingering) occurs — where a warm and salty layer initially lies above a colder and fresher layer [Stern, 1960]. Williams [1975], by measuring refractive indices,

observed salt fingers at the interfaces of Tyrrhenian Sea staircases. In the ocean, the results of these processes appear as horizontal layers with staircase-like shapes of temperature and salinity when plotted as a function of depth. Between a few meter-thick interfaces with strong thermohaline gradients, there are well-mixed layers that are several tens of meters thick [e.g. Schmitt, 1987; Schmitt, 1994; Radko, 2005; Schmitt, et al., 2005]. Observations have shown that the Tyrrhenian hosts up to ten largely homogenous layers with thicknesses of 50 to more than 500 m [Zodiatis and Gasparini, 1996]. These layers are separated by steps in temperature and salinity of 0.04–0.17 °C and 0.01–0.04 $g \cdot kg^{-1}$, respectively. Zodiatis and Gasparini [1996] also report that over the period from 1973 to 1992 the general presence of the staircases persisted but the number reduced from 8–10 to only 4.

The detection and quantitative description of thermohaline staircases has conventionally been carried out by analyzing data from multiple adjacent CTD stations, with Schmitt et al [1987] first showing T-S changes within the staircase layers. In the Tyrrhenian Sea, CTD locations—which may be separated by up to 200 km (when drawn in a waterfall diagram)—suggest laterally continuous well-mixed layers [Zodiatis and Gasparini, 1996; Figure 5 therein]. In a θ-S diagram the potential temperatures and salinities from the layers form distinct clusters or even linear segments in cases of variations along the well-mixed layers. However, the exact process through which the layers connect over a distance of up to 200 km is not well-understood.

Since double-diffusive processes by themselves would erode vertical gradients of temperature and salinity over time, a permanent resupply of heat and salt to the warm and salty water mass above, and a permanent thermohaline sink for the colder and fresher water mass below, are required to maintain the staircase structure. Horizontal advection of heat and salt by a slow-moving current through the well-mixed layers between the staircase steps has been proposed as the most likely candidate [Zodiatis and Gasparini, 1996]. In the case of the Tyrrhenian Sea then, it is the cyclonic intermediate LIW boundary current that supplies heat and salt to the system of thermohaline staircases. The layer underneath the staircases, the TDW, should in turn act as a thermohaline sink. For the system to be quasi-stationary the TDW–WMDW exchange with the Algero–Provencal Basin through the Sardinia Channel must remove the downward salt and heat flux inside the Tyrrhenian Sea. The interplay between the boundary currents and the persistent staircases in the center of the basin, and the balance of the vertical fluxes between the two water masses at the top and at the bottom of

the staircases, is however still poorly studied and documented because the heat and salt fluxes are small and therefore are difficult to determine.

Thermohaline staircases have been imaged using SO by numerous authors including Biescas et al. [2008], Krahmann et al. [2008], Buffett et al. [2009], Biescas et al. [2010], Fer et al. [2010], and Quentel et al. [2011]. Fer et al. [2010] documented an anomalously low internal wave field for staircases in comparison with adjacent measurements (e.g. for more dynamic regions such as eddies/meddies).

3 Data and methods

3.1. Seismic data

The seismic data were acquired as part of the MEDOC-2010 survey [Ranero et al., 2010], completed in April–May 2010, with the Spanish vessel R/V Sarmiento de Gamboa. It was a project designed to address the geological formation of rifted tectonic margins by utilizing both refraction and reflection seismology [e.g. Moeller et al., 2014, Prada et al., 2014]. Seismic acquisition parameters are shown in Appendix 1.

The MCS acquisition configuration consisted of a towed impulsive air source and a cable hosting the hydrophones (a ‘streamer’) deployed at a depth of several meters. The signal of the source’s wave front is recorded by the hydrophones after reflecting from acoustic impedance contrasts within the ocean and the solid earth.

It is important to note that due to the fact that the seismic oceanography component of this survey was a secondary objective, we could not customize the acquisition parameters for oceanographic targets. As a caveat then, the most prominent shortcoming of data quality is the ‘wrap-around multiple’ noise that was a result of the close shot spacing. That is, for a given ‘shot record’ from a single impulsive air source, the sound propagating in the water column from the previous shot didn’t have sufficient time to dissipate before the next shot started recording.

True amplitude seismic data processing was carried out post-cruise at GEOMAR. Technical details can be found in Appendix 2.

290

291 3.2. Oceanographic data

292

293 During seismic acquisition, we deployed 192 Lockheed Martin Sippican® T5 XBT probes
294 along-track from the R/V Sarmiento de Gamboa. XBTs have a vertical resolution of 65 cm
295 and an absolute temperature accuracy of +/− 0.07 °C [Boyd and Linzell, 1993]. We planned
296 the deployment of the XBTs to sample the temperature structure of the central portion of the
297 basin, where thermohaline staircases had been previously reported [Zodiatis and Gasparini,
298 1996]. The XBT probes were launched starting on 28 April 2010 being deployed in 6
299 segments across the 3 seismic sections — two segments per line covering the deepest parts of
300 the Tyrrhenian basin (Figure 1 and Appendix 1). Within each segment, probes were launched
301 at 15 minute intervals (approximately every 2.25 km).

302

303 As part of the OSMART (Oceanografía Sísmica en el MAR Tirreno) complementary action
304 to the MEDOC-2010 experiment, but not precisely simultaneous or coincident with the
305 seismic reflection acquisition, we also deployed CTDs from the vessel R/V Urania [Ranero et
306 al., 2010]. The salinity measurements from the CTD data provide an extra constraint to
307 improve the accuracy of the sound speed model for seismic data processing. Following the
308 procedure outlined by Papenberg et al. [2010] the CTD data were also used to derive salinity
309 values for the XBT profiles, which in turn allowed us to calculate potential temperatures that
310 remove the pressure effect on temperature.

311

312 Finally, in conjunction with the seismic, XBT and CTD acquisitions, we deployed an
313 autonomous underwater glider, manufactured by Teledyne Webb Research. The deep Slocum
314 glider (provided by GEOMAR) was used to measure temperature and salinity (and other
315 variables). It was released on 21 April 2010 off Naples, Italy from a locally rented boat. The
316 glider was steered in a westerly direction about one-mile north of seismic section EF (XBT
317 segment EF-2). It reversed course on 27 April 2010 being overtaken by the R/V Sarmiento de
318 Gamboa on 28 April 2010. It finished the section on 2 May 2010 (Appendix 1) to be
319 recovered eleven days later off Naples. The autonomous glider was programmed to dive to its
320 maximum depth of 1,000 m to cover as much of the staircases as possible. Collecting data
321 during descents and ascents, a horizontal resolution of about one slanted profile every 3 km
322 was achieved. The glider's CTD data were post-processed following the procedures
323 documented in Thomsen et al. [2016].

Herein we follow oceanographic convention and refer to a 'profile' as a one-dimensional measurement or data set along the vertical axis and 'section' for a set of horizontally consecutive profiles. Therefore, we refer to the seismic data as sections, not profiles, or lines, as is convention in seismology.

4 Results

The seismic sections cover the four water masses outlined in Section 2.1: AW, WIW, LIW, and TDW (Figure 2). Geologically, they span the Western Tyrrhenian Passive Margin, the Central and Southern Tyrrhenian Oceanized Crust and the Eastern Tyrrhenian Passive Margin [Marani et al., 2004]. The center of the basin is floored by exhumed mantle rocks that are covered by Plio-Quaternary sediments [Prada et al., 2015]. The Tyrrhenian basin is a region of well-known recent tectonic activity with an elevated crustal heat flux [Davies and Davies, 2010].

The imaging of the AW nearest to the surface is limited by the acquisition configuration (towed at a fixed depth), and by the imperfect attenuation of the direct wave. To optimally image the shallowest waters (less than 50 m), one needs to employ a customized acquisition system [e.g. Piété et al., 2013; Sallarès et al., 2016].

We acquired the seismic sections and the along-track XBT profiles accounting for marine operational logistics. Thus, sections EF and IJ happened to be acquired from west to east, whereas GH was acquired east to west. This is worth noting because, unlike a seismic image of the solid earth, the ocean circulates during acquisition [Klaeschen et al., 2009; Buffett et al., 2012], making the seismic image only a quasi-instantaneous snapshot of the subsurface. For the particular case of our survey, we expect that most dynamics occur in the upper waters, where circulation is faster and more widespread. In contrast, due to the nature of the deeper thermohaline staircases, we consider them to be for the most part stationary [Zodiatis and Gasparini, 1996] with respect to the vertical and horizontal scales imaged and at an acquisition rate of about 2.5 m/s. For comparison, a high-resolution reanalysis of the Mediterranean Sea [Pinardi et al. 2015] indicates maximum velocities of 0.3 m/s near the surface and 0.05 m/s at the depth of the staircases. All seismic sections contain some vertical

noise banding (see Sections 3.1 and Appendix 2), which overprint the oceanic signals in some areas (e.g. directly under km-10 in section EF).

In the following sub-sections, we describe the three seismic sections from north to south (EF, IJ and GH, respectively; Figures 1 and 2). We describe each section from west to east, divided into zones that are based on gross changes in thermohaline finestructure (see Figure 2). The intensity of the seismic reflectors in the images represents the amplitude of seismic wavelet peaks or troughs; higher intensity means more reflected energy. Energy is reflected more efficiently from sharper acoustic impedance contrasts — that is, sharper thermohaline gradients.

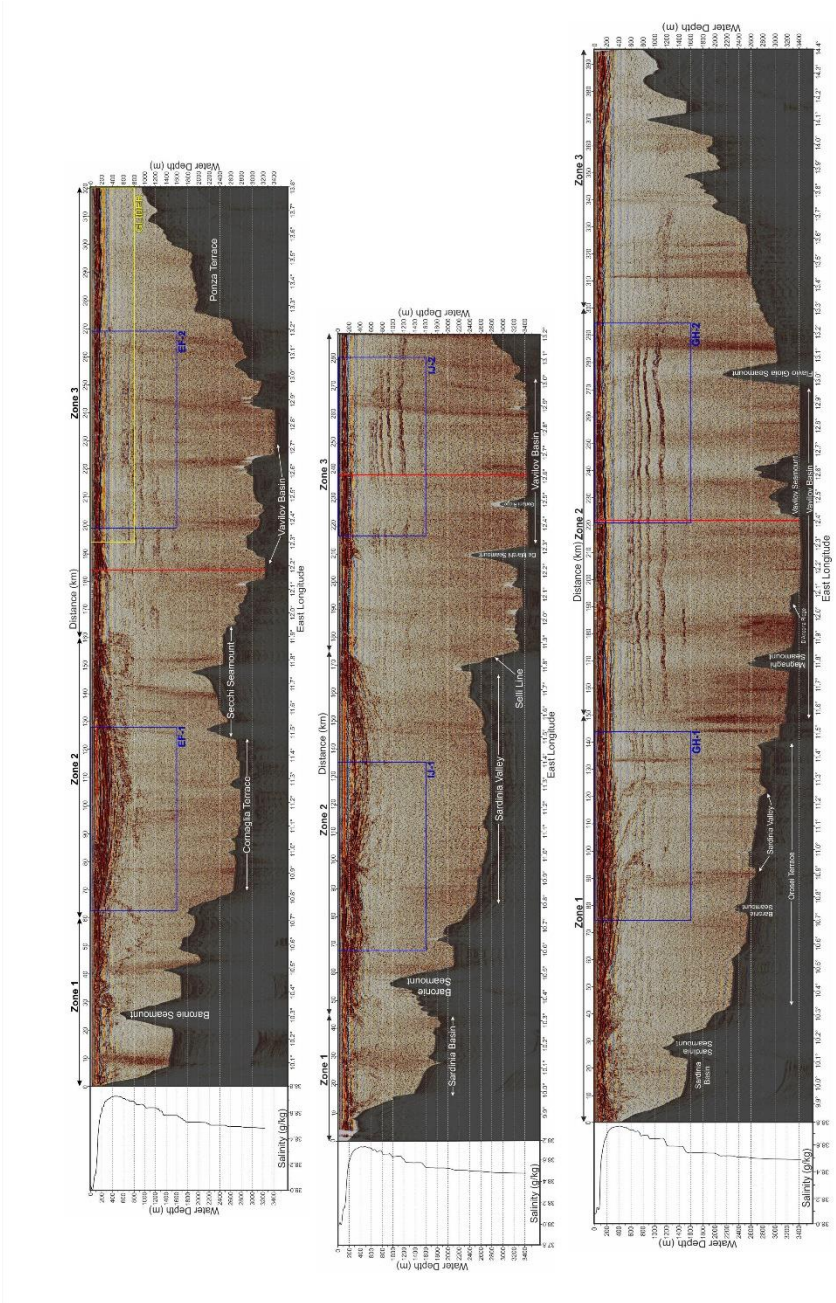

Figure 2: Full seismic sections displayed in true relative sizes. From top to bottom, section EF, IJ and GH. Blue boxes indicate the position of XBT deployments. Yellow box shows the location of the autonomous glider deployment. Red vertical lines indicate positions of CTD profiles shown on the left side of each seismic section. Sea floor features are indicated. Appendix 5 contains the seismic images in high-resolution A3 PDF format to view or print.

4.1. Seismic section EF

Zone 1 is characterized by near-horizontal wavy reflectors that appear to interact with the Baronie Seamount (e.g. near km-26). The shallowest reflectors become more horizontal in the east (km-40 to km-60). There is a V-shaped band of moderate energy reflectivity (km 40–70, depth 400–1100 m) that spans into Zone 2. In the deepest parts of Zone 1 there is only very weak reflectivity.

In Zone 2 we observe a large eddy at the surface that is centered at km-105. It has a maximum depth of 800 m and a diameter of about 90 km. The location of this eddy coincides with the location of the NTA [Rinaldi et al., 2010]. The strongest reflections of the eddy (at a depth of 350 m at km-100) are very laterally coherent. There is low reflectivity in the eddy's core (Figure 3a), similar to what is observed in Mediterranean Water Eddies (Meddies) in the open North Atlantic Ocean [Biescas et al., 2008]. Also noteworthy is the drop in reflector strength and lateral coherency at the base of the eddy (at about 700 m), possibly an indication of mixing with the underlying LIW layer.

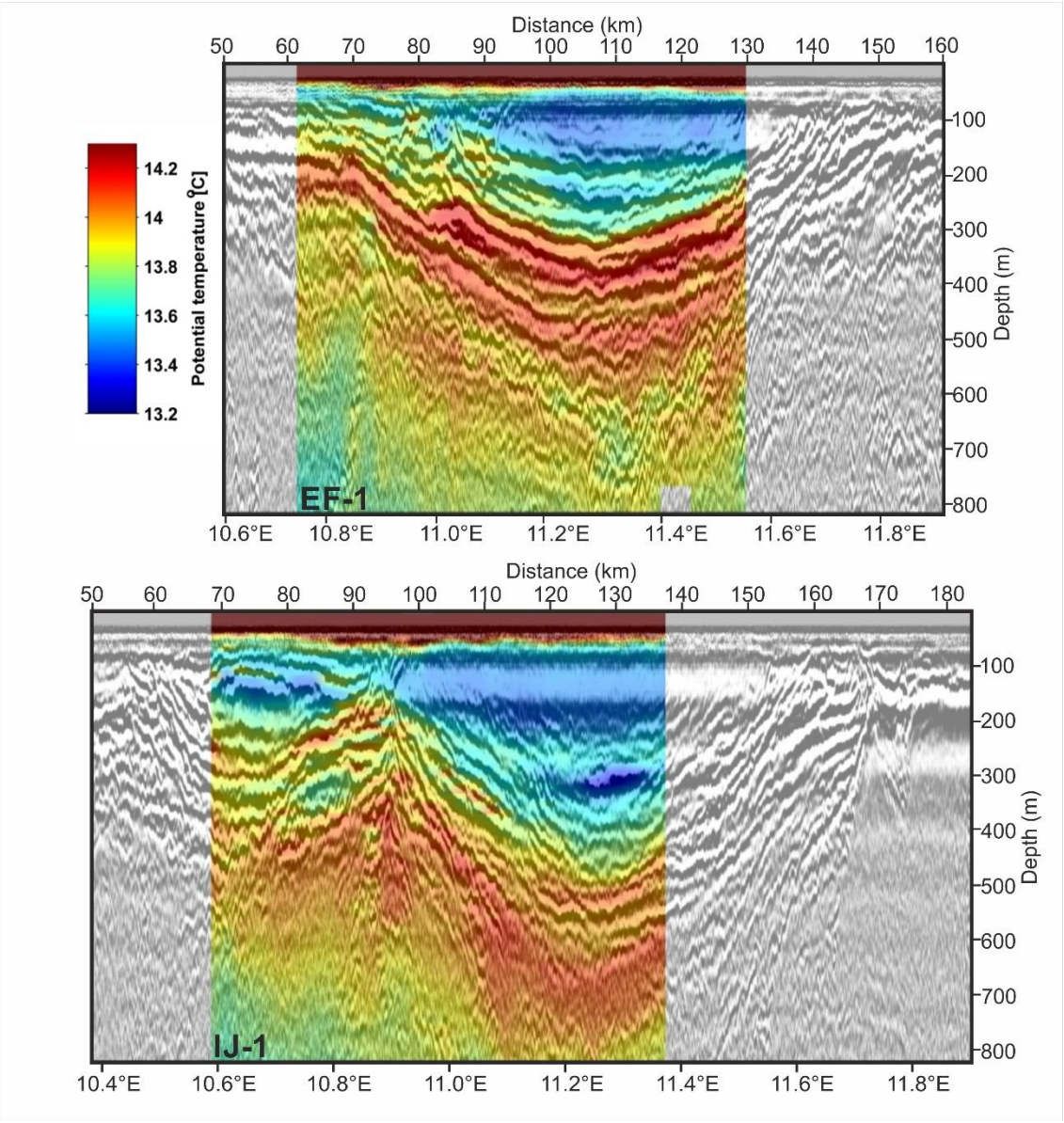

Figure 3 – a) a portion of seismic section EF showing a near surface eddy, b) part of seismic section IJ showing the same eddy, and a smaller eddy to the west. Shown in black and white shading are the seismic reflection data and in color the XBT temperature observations. Spatial scales and longitude coordinates are indicated. Lateral extents of eddies shown in this figure are depicted as white segments in the inset of Figure 1.

In Zone 3 at AW depths (0–200 m) there are strong near-horizontal-to-horizontal reflections. This AW overlies a seismically semi-transparent depth interval that extends from 200 to about 550 m. It shows both higher temperatures and salinities (Figures 4 and 7), corresponding well to the depth range of the LIW core. Below 550 m depth there are at least 6–7 continuous reflectors at depths of approximately 550, 600, 700, 800, 950, and 1200 m

that outline the thermohaline staircases. They vary in intensity from very weak to moderate. The staircase steps increase in separation as a function of depth (Figure 4). This increasing separation has been documented by Zodiatis and Gasparini [1996]. Also in agreement with Zodiatis and Gasparini [1996], we find that the reflectors are less continuous near the continental margins. Beneath the eddy we note very weak-to-vanishing staircases (Figure 2).

XBT (Figure 4) and glider data (Figure 7) indicate that these uppermost reflectors are caused by the halocline between the fresher AW and/or WIW and the saltier LIW. While there are also temperature gradients at the same depth, the reflectivity here is mostly caused by the strong salinity difference between the water masses. The XBT measurements collected together with the seismic data show that the eddy core is composed of relatively cold waters (Figure 3a); about 0.8 °C colder than the surrounding waters. The XBT data for segment EF-2 (Figure 4) shows a colder layer at about 80 m depth (km-197 to km-212) that likely represents the WIW. It spatially correlates to an area of weaker reflectivity below in the upper 3–4 staircase layers, and there is subtle evidence of an eddy-shaped structure here. Note here the down-dipping reflectors under km-180, and the up-dipping reflectors at the top of the staircase layers. On the other side (under km-215) there is a similar pattern. To the east of km-215 there are several other small zones of what must be warmer LIW eroding the upper staircase reflectors; they also have some correspondence with a cooler (WIW) layer above.

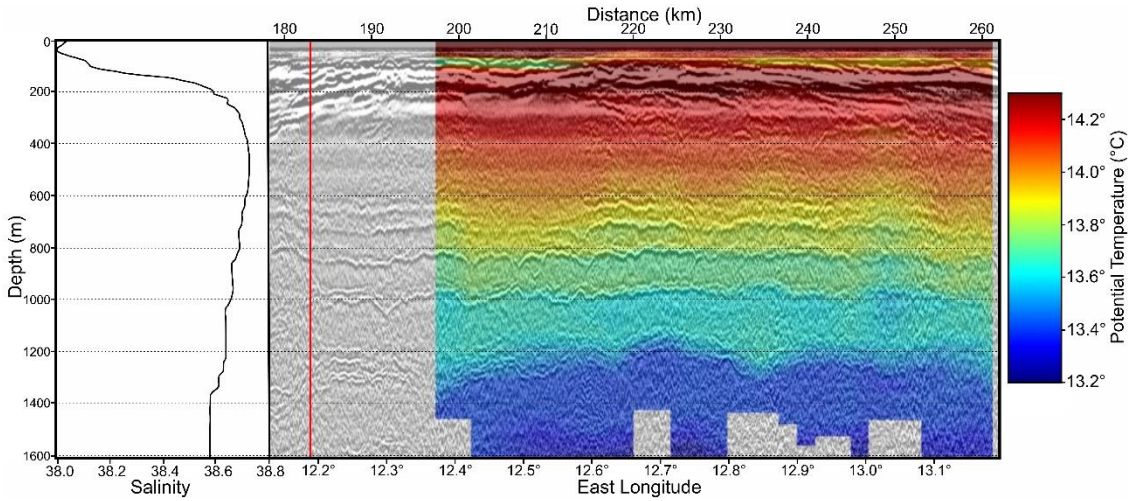

Figure 4 – Tyrrhenian Sea thermohaline staircases for XBT segment EF-2 and the nearest CTD profile (left) showing a correlation with the thermohaline staircase steps. Red line indicates corresponding longitude of CTD; for its precise location refer to Appendix 1. Shown in black and white shading are the seismic reflection data and in color the XBT

temperature observations. Spatial scales and longitude coordinates are indicated. See also Figure 1.

4.2. Seismic section IJ

Zone 1 is characterized by sloping reflectors on the continental shelf of Sardinia and a deep eddy-like structure in the deeper Sardinia basin. The interface between AW/WIW and LIW is visible as nearly continuous high amplitude reflectors. Strongly sloping reflectors are located on the shelf break at depths of 400–800 m (km-15). Reflectors with the opposite slope are visible at about km-23 and possibly at km-43. We interpret these as signs of an intermediate boundary current of LIW and an offshore return flow; though this could also be a mode-water eddy formed by LIW. Unfortunately, we lack other measurements in order to determine its zonal range.

Zone 2 is dominated by vertically depressed, high amplitude AW/WIW-LIW boundary reflections that can be subdivided into two eddies at around km-100. The western eddy is smaller with a size of about 40 km at this latitude, reaching a maximum depth of 500–550 m. This eddy has depressed reflectors at its lower side but uplifted reflectors at its upper side, which classifies it as a mode-water eddy. The eastern eddy has a size of about 75 km and does not show any reflectors at its top, indicating a regular surface eddy. It is still laterally coherent at depths of 600 m. In the depth interval from 600–1,000 m, there is some weak-to-moderate reflectivity that seems to be the disrupted continuation of the dipping reflectors at the western and eastern edges of this eddy. Within the same depth interval and further down, there is a weak impression of reflectors that might be the continuation of the regular staircase reflectors in Zone 3. These appear to follow the bowl shape depression of the strong reflectors above 600 m depth.

In Zone 3 we see near-horizontal-to-horizontal high energy reflectors that are generally confined to the upper 200 m of the water column, delineating the lower boundary of AW. At these shallow levels, there is an obvious change: from km-175 to km-205 the near-surface waters are very horizontal and do not quite reach 200 m depth. Below this layer there is barely any discernible reflectivity until about 700 m where there are weak-to-vanishing near-horizontal staircase reflectors. These weak reflectors appear to be pushed down similar to what seems to occur below the large eddy. At km-205 there is an abrupt change in reflectivity dip in the shallow waters (which continue with slightly less horizontal coherency until km-

290); it spatially correlates to a sharp increase in reflector energy and lateral coherency for the depths of 600–1,300 m. This change coincides with the peak of the De Marchi seamount. At km-220, again the staircase reflectors are barely detectable, but they do seem to be vertically depressed in the center (km-227), and they correlate with the peak of the Gortani Ridge. Biescas et al. [2010] document the interaction of staircase layers at the top of the Gorringe Bank in the North Atlantic, although at much closer scales. In our study, the spatial correlation of the seamounts to the staircase coherency and amplitude, raises the question of whether interaction with these features could possibly disturb the staircases at this depth. At about km-232, the staircase reflectors steepen moderately to join with high amplitude, high laterally coherent staircase reflectors, which are observed to continue until km-290 — but with the upper reflectors more degraded. The prominent reflector at almost 1,200 m depth is split into two or more reflectors in some places. There is a weaker, double reflector with a lateral coherency of only 20 km observed at 1,500 m. Below 1,500 m, there is almost no detectable coherent reflectivity.

The near-surface reflectors in the depth interval from 50–200 m (lower boundary of AW) show the same bimodal arrangement as section IJ (eddies in the west/staircases in the east). EF and IJ bisect two large adjacent surface eddies (Figure 3ab), which, given their cold cores (below 13.4 °C) and locations, seem to neatly outline the NTA. In the upper 700 m of the water column of section IJ (Figure 3b), like section EF, we observe the lower boundaries of AW and WIW as a package of high acoustic impedance reflectors, which vary in intensity and depth. The corresponding XBT data reveal an abrupt increase in temperature of 1.0 °C until a maximum depth of about 700 m at the center of the eddy. Temperatures then decrease with depth until at least the bottom of the XBT profiles at about 1,600 m. Section IJ shows a deeper eddy, suggesting that it has been bisected closer to its center (assuming it is symmetrical). This is also in agreement with chlorophyll satellite data acquired during the same period (Appendix 3).

As with section EF, the LIW core does not exhibit strong reflectivity across the whole section. In the depth interval from 600–1500 m between the LIW and TDW cores there is little reflectivity under the eddies; the reflectivity becomes much more apparent in the eastern portion of the section, between km-220 and the continental shelf. Across that same zonal range, the staircases are more continuous and coherent than section EF. However, the steps do also increase in separation as a function of depth.

XBT segment IJ-2, like EF-2 shows warmer shallow waters as well as temperature steps corresponding to the thermohaline staircases. There is a notably warmer layer (+0.2 °C) that protrudes into the top of the staircases between km-223 and km-236, an area with very low seismic reflectivity (Figure 5). The MCS data here show clear indicators of a symmetrical eddy-like shape (note the up- and down-dipping reflectors below approximately km-210 and km-245 seen at this vertical exaggeration, which give the eddy a circular shape). Above this warm area, the XBT data have a distinctly cooler layer centered around 100 m, probably WIW. Again, like section EF (Figure 4), there is a spatial correlation between the location of the WIW layer and the warmer, deeper layer that protrudes into and seems to erode the staircases; in this case, the erosion is much more obvious than in section EF. Elsewhere there is a good correlation between the XBT temperature data and the staircase steps (Figure 5).

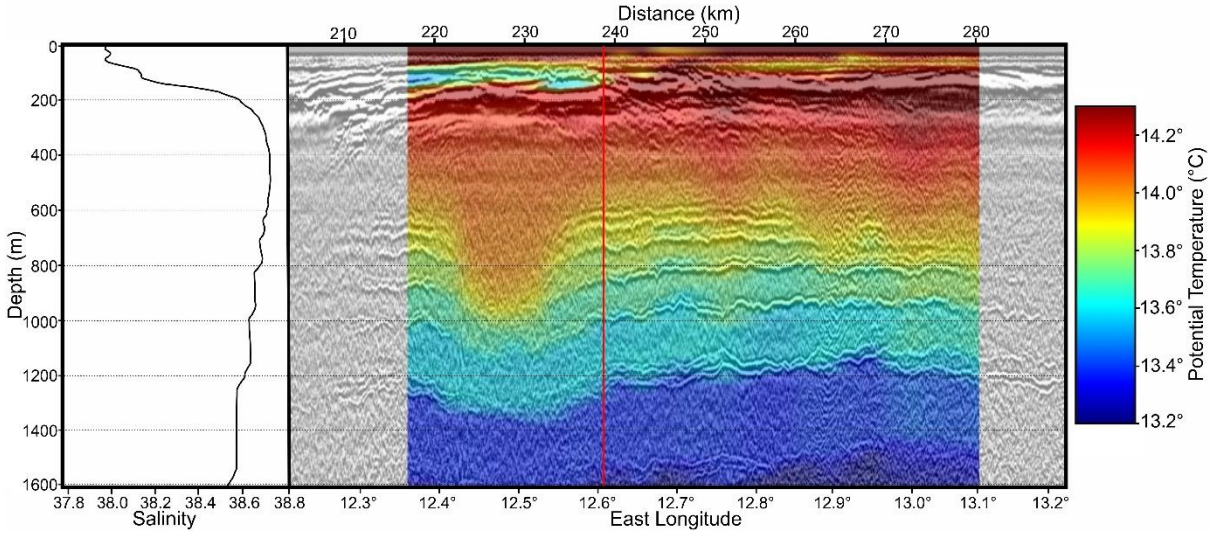

Figure 5 – Tyrrhenian Sea thermohaline staircases for XBT zone IJ-2 and the nearest CTD profile (left) showing a correlation with the thermohaline staircase steps. Red line indicates corresponding longitude of CTD; for its precise location refer to Appendix 1. Shown in black and white shading are the seismic reflection data and in color the XBT temperature observations. Spatial scales and longitude coordinates are indicated. See also Figure 1.

4.3. Seismic Section GH

In the vicinity of the Sardinia margin the upper AW waters of Zone 1 (within the upper 200 m) are characterized by high energy, laterally discontinuous, near-horizontal reflectors, which become progressively continuous going eastward. Toward the eastern portion of Zone 1 the

AW reflectors reach depths of up to 400 m, possibly demarcating the southern flank of the eddies seen in EF and IJ. Here, there are also near-continuous down-sloping filaments of reflectivity that reach to depths of up to 800 m and make contact with weak-to-moderate energy staircase reflectors. Without other corroborating data, it is unclear what thermohaline boundary causes these sloping reflectors. The weakly visible regular staircases in Zone 1 decrease in amplitude toward the western continental slope, where they are barely detectable.

Zone 2 defines the location of the most reflective and laterally coherent staircases of all three seismic sections. Like sections EF and IJ they are characterized by increasing step separation as a function of depth. Of the 6–7 staircase steps, the most reflective ones occur between km-235 and km-290 at depths of 600–1200 m. In this part of the staircases one of the deeper reflectors (1000–1200 m) splits into two. The eastern part of these staircases (between about km-260 and km-285) appears to rise over the Flavio Gioia seamount.

Zone 3 is defined based on the abrupt drop in both reflectivity and lateral coherency of the staircase steps. In Zone 3 the staircases are barely detectable, being weaker at the top than at the bottom, and they appear to be vertically depressed toward the eastern edge (km-330). Further eastward of km-340, over the continental shelf, the staircases are no longer detectable. This is possibly the result of the more variable topography on which the boundary current would create a turbulent regime that is not conducive to the formation of staircases.

The XBT segment GH-1 (not shown), barely outlines the edge of the cold-core eddy. But there is some correspondence between temperature and the dipping filaments. GH-1 shows the warmer near-surface waters and is relatively laterally uniform. There is a good agreement between the XBT-derived temperature and the thermohaline staircase stratification of the seismic data.

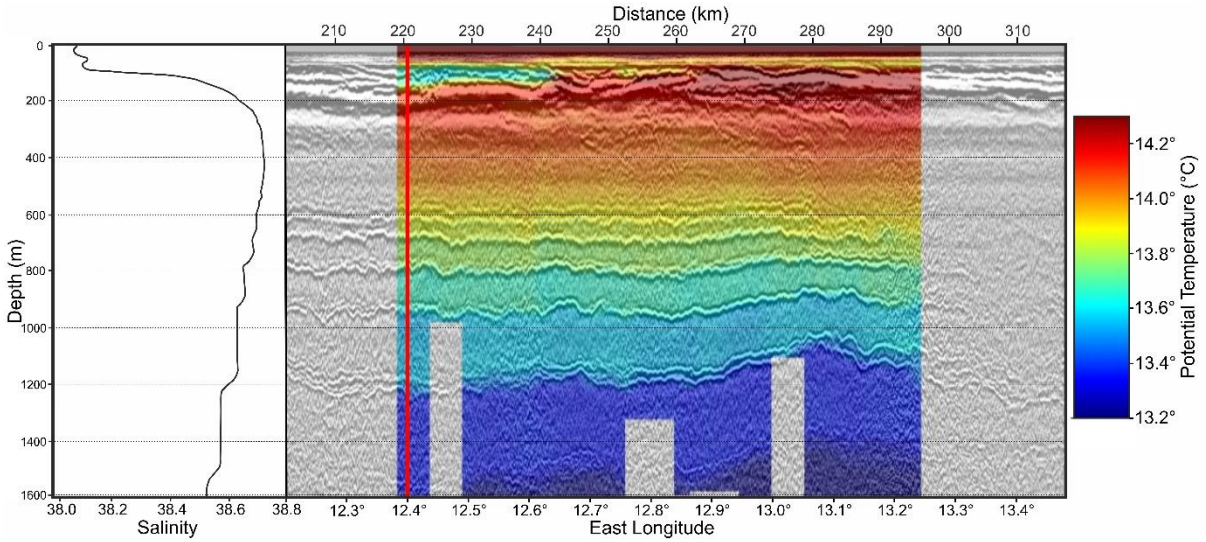

Figure 6 – Tyrrhenian Sea thermohaline staircases for XBT zone GH-2 and the nearest CTD profile (left) showing a correlation with the thermohaline staircase steps. Red line indicates corresponding longitude of CTD; for its precise location refer to Appendix 1. Shown in black and white shading are the seismic reflection data and in color the XBT temperature observations. Spatial scales and longitude coordinates are indicated. See also Figure 1.

The XBT and CTD data for segment GH-2 show an excellent correlation with the seismic staircase steps, having an approximately 0.2 °C difference between adjacent mixed layers. In the same zonal range as IJ-2 there is a cooler layer at about 100 m depth. There is minimal disturbance of the staircases in what seems to be the most quiescent part of the sea that we observed.

4.4. Autonomous glider results

We make use of glider data to corroborate the seismic data with in situ measurements of salinity (Figure 7). Although the glider used here unfortunately was not designed to reach the depths of the deepest thermohaline staircases in the Tyrrhenian Sea, it was able to reach the upper four steps. The glider's CTD provided local and near-simultaneous measurements of salinity that were in good agreement with ship-based CTD measurements of salinity used to calculate the sound speed distribution. Figure 7 shows glider-observed salinities overlaid on seismic data for the eastern part of seismic section EF. The data show a low salinity zone (36.9–38.2 $g \cdot kg^{-1}$; mean 37.9 $g \cdot kg^{-1}$) that corresponds to the AW in the upper approximately 200 m. The LIW displays the highest salinity values in this section, reaching as high as 38.75

574 g·kg^{-1}. As already described, there is only weak seismic reflectivity within the LIW layer.
575 Below the LIW, the glider salinity values correspond well with the reflective staircase
576 boundaries, showing step-like decreases of salinity, and of course temperature (not shown), at
577 the interfaces between the well-mixed layers.

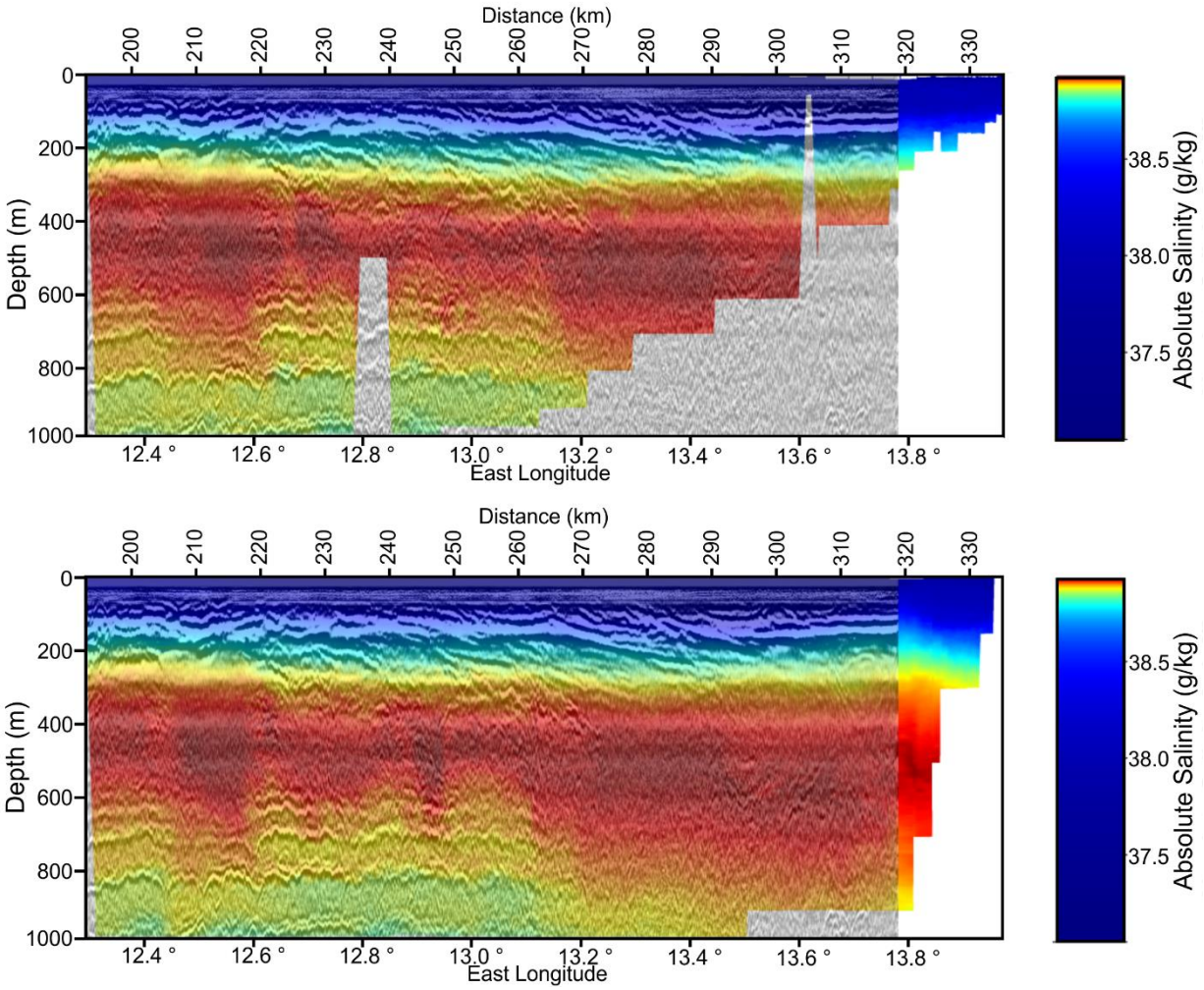

578

579 Figure 7 – Salinity data from autonomous glider mapped over greyscale seismic data. Top
580 panel is outbound measurement. Bottom panel is inbound measurement. See Figures 1 and 2
581 and Appendix 1 for location.

582

583

584 **5 Discussion**

585

586 5.1. Meso-scale eddies

587

588 Eddies have previously been observed in the Tyrrhenian Sea [e.g. Budillon et al., 2009,
589 Iacono et al., 2013]. We observe two connected anticyclonic eddies reaching down to at least

400 m (Figures 3a and 3b), one of which we identify as part of the quasi-permanent NTA [Rinaldi et al., 2010, Iacono et al., 2013]. The eddies are outlined best in seismic sections EF and IJ. With just three seismic sections separated by 20–30 km, we have limited north-south spatial resolution. Yet, two joined structures are clearly visible in section IJ (Figure 3b). The larger of the two, is also present in the seismic data of section EF. There is no clear bowl-shaped signature of it in section GH, but it possibly samples the southern edge of the NTA (e.g. between km-30 and km-170). At the corresponding longitude range of the NTA there are some filament structures that contact the staircase layers, and we speculate that they may have been induced by the eddy.

Assuming a symmetrical shape for the eddy, we estimate its center to be located between sections EF and IJ, somewhat closer to IJ. Satellite imagery of a zone of low chlorophyll concentration at the sea surface (Appendix 3) shows a good spatial correlation with the eddy in the seismic data. The chlorophyll anomaly is an average of five 8-day mean fields around the time of the seismic surveys and shows an anticyclonic circulation shape. It appears that north of the low chlorophyll concentrations, a high chlorophyll anomaly is being dragged from the coast of Sardinia into the eddy. Both the chlorophyll and the seismic data suggest a diameter of at least 70 km. The seismic data of section IJ near the eddy's center show the first reflectors at about 300 m depth whereas in the non-eddy parts of the section they occur at about 100 m depth. This is a clear sign that the eddy's core was formed by a thickened rather homogeneous layer of WIW. Below this core, we find a nearly 300 m thick layer with reflectors that all appear to follow the classical bowl-shape of an anticyclonic surface eddy. This uppermost layer of reflectors is significantly thicker than in the non-eddy parts of the sections. This is likely caused by the strong temperature gradient between the very cold WIW of the eddy cores and the underlying warm LIW layer. In the remainder of the sections no cold WIW layer is present and the vertical temperature gradient between AW at the surface and LIW is much weaker, thereby reducing one of the possible causes for the reflectors. The bowl-shaped reflecting layers of the eddy reach depths of 700 m. In Zone 3 of the same section we find clean horizontal staircases at that depth. There appear to be some traces of staircases at the western side of the eddy but they are more diffuse. This suggests that the eddy's advection has an adverse effect on the horizontal continuity of the double diffusive staircases.

624 5.2. Thermohaline staircases

625

626 The seismic data of the staircase depth interval are shown in Figures 4, 5 and 6 for sections
627 EF, IJ, and GH, respectively. The depths of the temperature steps observed on the XBT,
628 CTD, and glider data match the depths of the high acoustic impedance contrasts that reflect
629 sound between approximately 600 m and 1,900 m. This confirms that these horizontally
630 extensive seismic contrasts are in fact a result of thermohaline staircases. Zodiatis and
631 Gasparini [1996] previously documented the horizontal extension of the Tyrrhenian
632 thermohaline staircase area to be at least 150 km. Their study was based on a set of CTD
633 profiles and they were able to infer the horizontal coherency of the staircases only through
634 the consistent water mass properties within the well-mixed layers in profiles that were located
635 tens of kilometers apart. With the seismic data, we are able to clearly prove their continuous
636 coherency for up to 200 km with a profile (seismic trace) spacing of only 6.25 m. The very
637 high horizontal sampling of the seismic data exposes small features such as the splitting and
638 recombination of steps over horizontal scales of just a few kilometers.

639

640 In general, the staircases are more laterally coherent toward the center of the Vavilov Basin
641 (e.g. the central part of section GH) and less so at the basin's margins, again confirming the
642 findings of Zodiatis and Gasparini [1996]. This distribution mirrors the general strength of
643 ocean currents at the depth of the staircases. Near the margins, the generally cyclonic
644 circulation of the basin is found in the form of boundary currents. In contrast, the central
645 basin has only weak circulation and thus persistent staircases can form. It appears therefore
646 that the boundary circulation prevents the extension of the staircases right up to the margins.

647

648 We also note that in the region of the most prominent staircases, the upper and lower
649 reflective steps tend to be more diffuse. This is simply a result of the weaker vertical
650 temperature and salinity gradients at the top and the bottom of the staircase depth interval
651 (see salinity profile in Figure 4). It contrasts with the staircases' center region over the
652 deepest part of the basin, where the reflectors form sharper boundaries. Towards the
653 continental shelf, reflectors are more diffuse. But in that case we think that turbulence
654 generated by the boundary current is the cause.

655

656

657 5.3. Internal Waves

Internal waves are a nearly ubiquitous feature of the oceans [Garrett and Munk, 1975, 1979]. Created by tides or atmosphere-ocean interaction, they can persist for long times and travel great distances. Measurements in the open ocean have found a consistent shape of the frequency and wave number spectra of internal waves [Garrett and Munk, 1975, 1979]. Wave-wave interaction is assumed to transfer energy from long wave lengths and periods to shorter ones until they become unstable and break [Müller et al., 1986, Thorpe, 1975, Sallarès et al., 2016], ultimately contributing to diapycnal mixing in the form of small scale turbulence. Seismic reflection data have been shown to be a useful tool to observe the vertical undulations of internal gravity waves and to derive spectra of their strength [Holbrook and Fer, 2005]. Horizontal wave number spectra of the energy density of these undulations agree well with the spectrum found by Garrett and Munk [1975, 1979]. Krahmann et al. [2008] applied the approach of Holbrook and Fer [2005] to data off the Iberian Peninsula and differentiated the results in the horizontal. There it showed that topographic and hydrographic features modified the overall strength of the internal wave field.

Here we performed the same analyses. The automated tracking algorithm of Krahmann et al. [2008] was run over all three seismic sections. To improve tracking in the relatively noisy seismic data a 9 CDP (56.25 m) running mean was applied in the horizontal direction. The algorithm identified 3545 (EF), 4357 (IJ), and 2996 (GH) traces of 256-CDP (1,600 m long) reflective layers — longer segments were separated into pieces — for the three sections, respectively. Comparable to Krahmann et al. [2008], we found track excursions at less than 50 m vertical separation to be significantly correlated (not shown). Accordingly, we reduced the number of independent tracks used in the uncertainty calculation. As the vertical excursions caused by internal gravity waves depend on the local vertical density gradient, a normalization is required to make the spectra at different locations comparable. We derived the normalization factor, the buoyancy frequency N, from the collected CTD data and applied it to the wave number spectra calculated from the raw depths of the tracks. In contrast to the data from Krahmann et al. [2008], the reflection data presented here covers a larger depth range and also shows reflectors in the upper water column. Since the buoyancy frequency varied significantly with depth (Figure 8), we found normalization factors ranging from 0.3 cph at 1,500 m depth to 3.3 cph at 100 m depth (compare that to 1.4 cph in Krahmann et al. [2008]). A single smoothed buoyancy frequency profile was therefore derived to normalize the spectra at different depths. The buoyancy frequency quite likely also varied along the

692 sections, particularly in the upper water column. Unfortunately, we do not have the required
693 horizontally resolved CTD data to create a horizontally variable normalization. The averaged
694 normalized wave spectra for the three sections are shown in Figure 9. The spectra are
695 remarkably consistent between the three sections and agree well with the shape expected
696 from the Garrett and Munk [1975] model. In contrast to the spectra reported by Holbrook and
697 Fer [2005] and Krahmann et al. [2008], all three show internal wave energy levels
698 significantly below the open ocean values of the Garrett and Munk [1975] model. The likely
699 cause is that, compared to other oceans, the weak tidal field in the Mediterranean Sea creates
700 only a relatively weak internal gravity wave field. More recent work by Holbrook et al [2013]
701 has shown that the horizontal wave number spectra from seismic oceanography sections can
702 be used to estimate mixing rates. The relatively high levels of noise in our data however do
703 prevent such calculations.

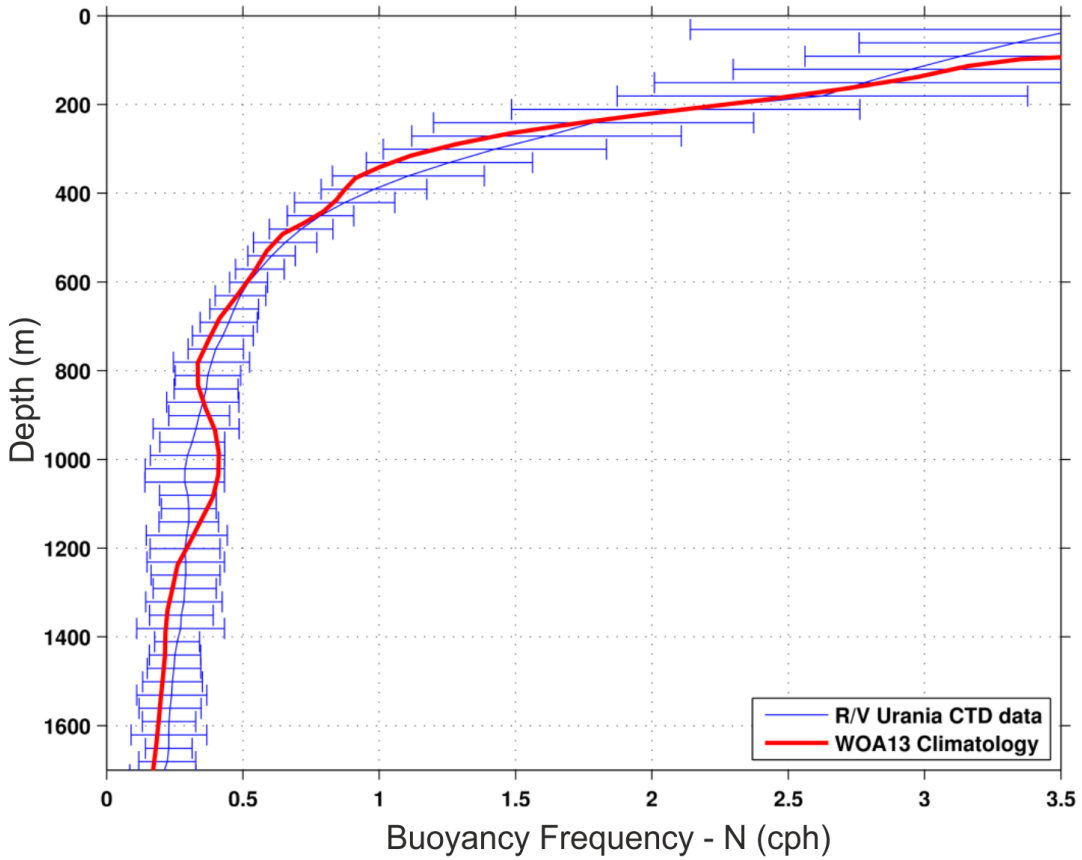

704

705 Figure 8: Smoothed buoyancy frequency profiles calculated from R/V Urania CTD data and
706 from WOA13 climatological data [Locarnini et al., 2013; Zweng et al., 2013]. The blue
707 profile was used to normalize the energy density spectra of vertical excursions of the

708 reflectors.

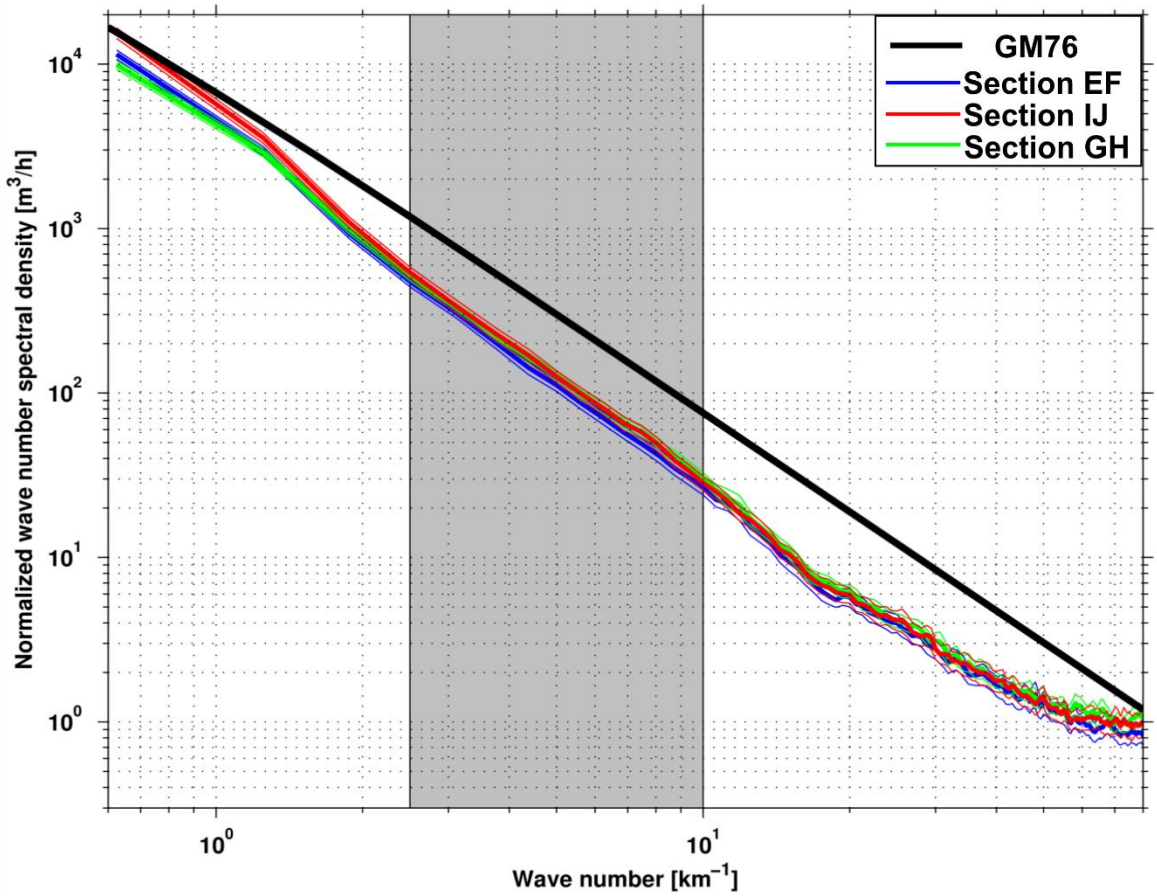

709

710 Figure 9: Average horizontal wave number spectra of normalized internal wave energy
711 density for the three sections. Also shown is the internal wave spectrum expected for open
712 ocean conditions, black line [Garrett and Munk, 1975, Katz and Briscoe, 1979] for the
713 latitude range of the three sections and for a buoyancy frequency of 2.0 cph. The gray area
714 marks the interval over which the spectra were integrated for the energy level comparisons.

715

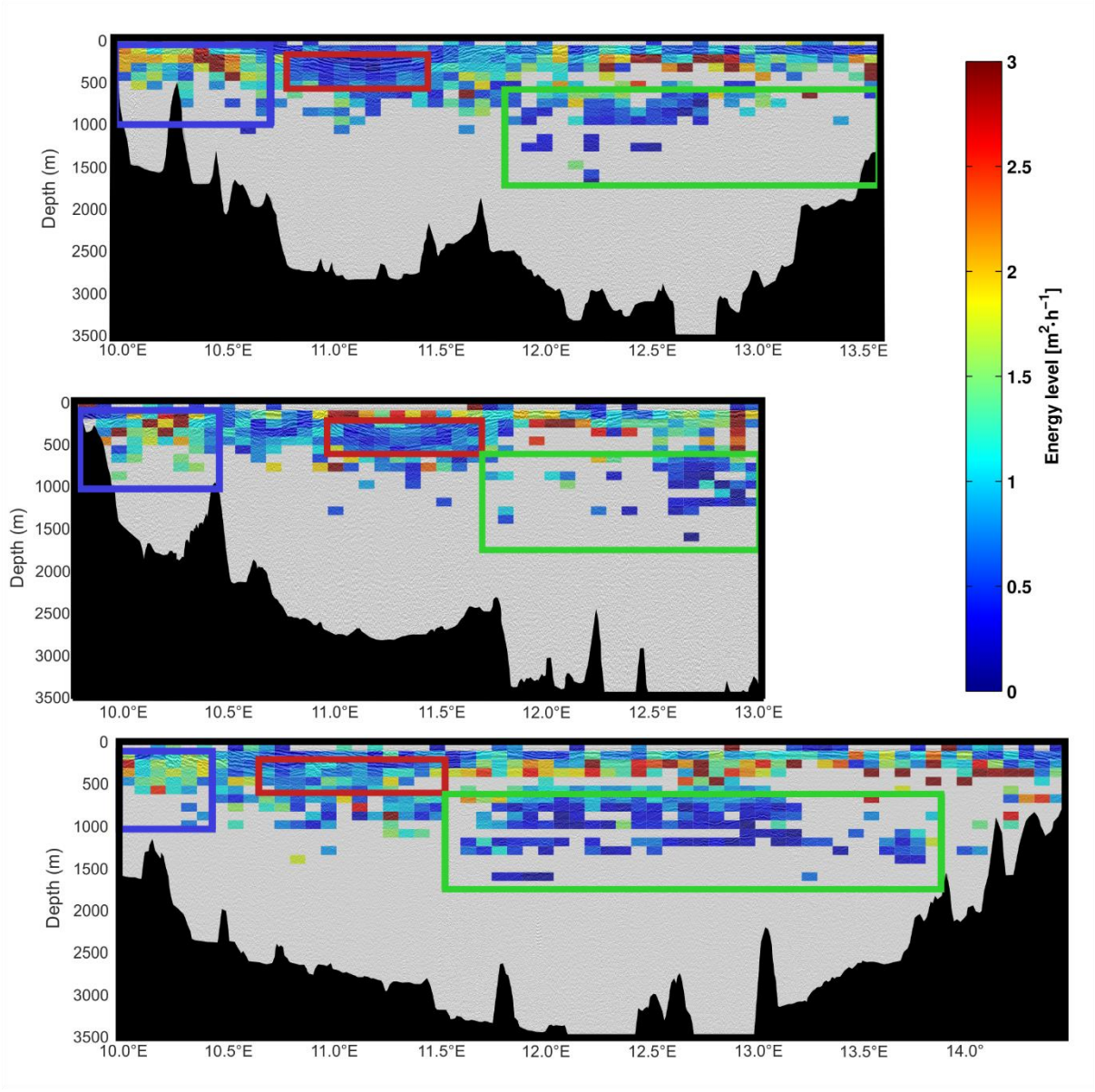

Figure 10: Internal wave energy levels ($m^2 \cdot h^{-1}$) averaged over 100 m thick depth intervals and 1000 CDP (6.25 km) wide horizontal intervals mapped over grayscale seismic data. The energy levels show distinct regional differences that appear to coincide with features found in the seismic reflection data. The three boxes in each panel show areas (blue: Sardinia shelf break region, red: eddy region, green: staircase region) over which the averages from Appendix 4 were calculated.

To further analyze the internal wave energies we integrated the energy over the interval from 100 to 400 m long waves. For each 256-CDP long tracked segment this gives an energy level of the internal waves. We then averaged these energy levels over 6.25 km long and 100 m thick intervals to determine possible regional variations (see Figure 10). Indeed we were able

728 to determine such variations. When shown together with the seismic reflection data the
729 variations in internal wave energy suggest connections with oceanographic features.
730 However, do to the lack of corroborating physical measurements and the limited horizontal
731 extent of our data these connections are only circumstantial.
732
733 In particular we find in each of the three sections two regions with low internal wave energy
734 levels. The first is the larger eddy in the western half of sections EF and IJ and to a lesser
735 extent in GH (marked by red boxes in Figure 10). There the energy levels are only about 70%
736 of the full-section averages (see Appendix 4). Even lower energy levels are present in the
737 deeper part of all three sections below 600 m where the continuous thermohaline staircases
738 are found (marked by green boxes in Figure 10). There the energy levels drop to 40% of the
739 full-section averages. In contrast to these low energy regions we find slightly elevated energy
740 levels (140% of the section averages) on the western side of the sections close to the coast of
741 Sardinia (marked by blue boxes in Figure 10). Unfortunately, the sections were terminated on
742 their eastern ends before the shelf break was reached. Thus, we are not able to confirm that
743 the elevated energy levels on the western shelf break have counterparts on the eastern side
744 where the cyclonic boundary currents are also present.
745
746 When plotted against depth (Figure 11), the energy levels of all three sections show a
747 significant decrease as a function of depth. Little difference can be seen between the sections.
748 If there are any differences, they can be explained by the presence of the eddy with low
749 energy levels. The vertical variation in the energy level we find here cannot be explained by
750 the vertically varying vertical density gradient because the spectra have been normalized by
751 the depth dependent buoyancy frequency. Without corroborating measurements we are
752 however not able to determine the cause for the vertical variation.
753

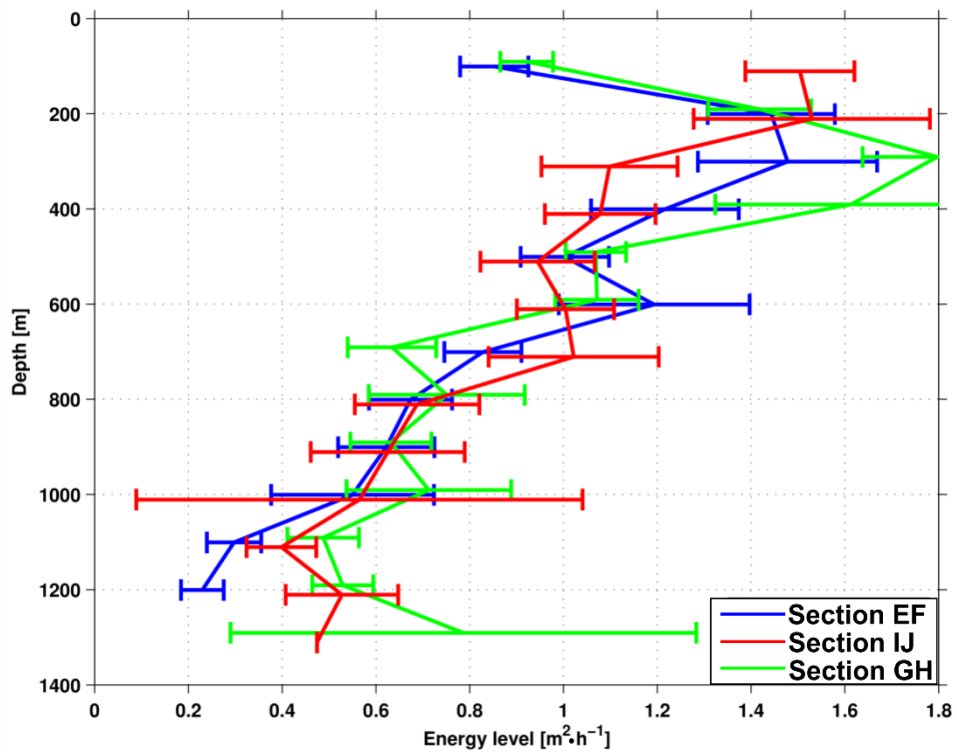

Figure 11: Average normalized internal wave energy levels of the three sections plotted against depth showing a distinct vertical variation.

The depth intervals and regions with thermohaline staircases (below 600 m in the central part of section GH and the eastern parts of sections EF and IJ) show particularly low energy levels with values of 0.3 to 0.7 $m^2 \cdot h^{-1}$ (see Figure 9 and Appendix 4). Compare that to the normalized value from Garrett and Munk [1975] for the latitude of 40° N of 2.5 $m^2 \cdot h^{-1}$.

Elevated energy levels are found at the western ends of the sections close to the coast of Sardinia (see Figure 10 and Appendix 4). Unfortunately, the sections were terminated on their eastern ends before the shelf break was reached. Thus, we are not able to confirm that the elevated energy levels close to the coast are caused by the cyclonic boundary currents.

6 Conclusions

We acquired and analyzed seismic oceanography data from the Tyrrhenian Sea and found several distinct shallow and deep features that have never been shown before in such high lateral detail. The images clearly delineate the boundaries between AW and LIW and between LIW and TDW.

In the northwestern part of the seismic sections we see two cold-core anticyclonic eddies likely formed of WIW. The larger of these eddies has been documented before as the NTA. The core of this eddy has a thickness of about 200–300 m and contains relatively few reflectors. Strong reflectors are found underneath the eddies down to about 700 m depth. Satellite images acquired during the period of the seismic acquisition show a chlorophyll minimum at the position of the larger eddy, in good agreement with our observations.

In the transition zone between LIW and TDW, vast areas of thermohaline staircases are imaged in unprecedented lateral resolution (6.25 m) continuously over the whole central Tyrrhenian basin. Their appearance is due to the pronounced temperature and salinity differences between the water masses that cause sound-reflecting impedance contrasts. Coincident XBT temperature, as well as temperature and salinity observations from both CTD and glider observations, match well with the seismic images, outlining the main water masses. We are able to trace seismic reflectors over distances of up to 200 km. These reflectors are caused by locally strong vertical impedance gradients. In the case of the staircase reflectors in the Tyrrhenian Sea (a regime with salt-fingering as the primary formation mechanism) we confirm that the impedance gradients are caused by temperature and salinity contrasts, with temperature being the dominant contributor as previously suggested elsewhere (e.g. Ruddick et al. [2009]; Sallarès et al., [2009]).

We find that some regions are better resolved than others, partially due to the fact that the high shot rate of the acquisition configuration introduced wrap-around multiple reflections that could not be fully removed without also degrading the overall data quality. Apart from this technical cause, for poorly resolved regions we find weak-to-vanishing staircase reflectors along the boundaries of the surveyed northern half of the Vavilov basin, while the reflectors in the center of the basin are the best resolved. Because circulation in the deep Tyrrhenian Sea is dominated by cyclonic currents limited to the basin boundary, our results

suggest that circulation inhibits the formation and/or persistence of thermohaline staircases. However, the boundary circulation also resupplies the Tyrrhenian Sea with the heat and salt that is required to balance the downward flux in the basin interior.

The analysis of the vertical excursions of the reflectors adds a second view, independent of the coherency of the reflectors. When analyzed for the spatial variation in internal wave energy we found distinct regional differences. Wherever coherent thermohaline staircases were present we found very low energy levels. This supports the view of a quiescent environment required for the staircase formation and preservation. Elevated energy levels were found near the boundaries of the basin and near the eddies, where water masses are more dynamic.

Our results show that horizontal exchange between the boundary and the interior region must obviously occur. It is however still unclear how exactly this takes place. The seismic, temperature and salinity data clearly show that in the center of the basin a very quiescent environment is conducive to the double-diffusive processes that form the extensive thermohaline staircases. However, to improve our understanding of the system, further analyses or new measurements of boundary current water masses feeding into the interior are required.

Acknowledgments and Data

This research was funded by the MEDOC project (seismic and oceanographic acquisition): Spanish Plan Nacional: CTM2007-66179-C02-01/MAR (Principal Investigators: C. R. Ranero and V. Sallarès) and Spanish Acción Complementaria OSMART CTM2009-07772-E (Principal Investigator: Francisco Machín); Grant George Buffett was funded through a Marie Curie Intra-European Fellowship (IEF): FP7-PEOPLE-2010-IEF. The glider operation was funded by the Deutsche Forschungsgemeinschaft (grant KR 3488/1-1). The authors would like to extend thanks to the captains and crews of the Spanish vessel R/V Sarmiento de Gamboa and the Italian vessels R/V Urania (Chief Scientist: Nevio Zitellini; Chief Scientist of oceanographic acquisition: Simón Ruiz) and Cormorano V. Thanks to Richard W. Hobbs and Ekaterina Vsemirnova for enlightening discussions. Chlorophyll data were obtained freely from neo.sci.gsfc.nasa.gov. Pierpaolo Falco of the Università degli Studi di Napoli "Parthenope" and his colleagues deserve a big thank you for managing the glider operation.

Seismic data were processed using Seismic Un*x [Cohen and Stockwell, 2001], Omega2© by WesternGeco©, and Globe Claritas© [Ravens, J., 1995]. Oceanographic data were displayed with Ocean Data View© [Schlitzer, R., 2013] and Generic Mapping Tools (GMT) [Wessel and Smith, 1998]. Seismic and oceanographic data are available at www.pangaea.de under doi:10.1594/PANGAEA.875602. Thank you to two anonymous reviewers for their constructive comments and helpful suggestions on an earlier version of the manuscript.

References

Artale, V., M. Astraldi, G. Buffoni, and G. P. Gasparini (1994), Seasonal variability of gyre-scale circulation in the northern Tyrrhenian Sea, *J. Geophys. Res., 99(C7)*, 14127–14137, doi:10.1029/94JC00284.

Astraldi, M. and G. P. Gasparini (1994), The Seasonal Characteristics of the Circulation in the Tyrrhenian Sea, in Seasonal and Interannual Variability of the Western Mediterranean Sea (ed. E. La Viollette), *American Geophysical Union*, Washington, D. C. doi: 10.1029/CE046p0115.

Barbosa Aguiar, A. C., C. Ménesguen, S. Le Gentil, and R. Schopp (2015), Cyclones and Anticyclones in Seismic Imaging, *J. Phys. Oceanog.*, 45(9), 2436-2443, doi: 10.1175/JPO-D-15-0066.1.

Biescas, B., V. Sallarès, J. L. Pelegrí, F. Machín, R. Carbonell, G. Buffett, J.J. Dañobeitia and A. Calahorrano (2008), Imaging meddy finestructure using multichannel seismic reflection data. *Geophys. Res. Lett.*, 35(11), doi:10.1029/2008GL033971.

Biescas, B., L. Armi, V. Sallarès, and E. Gràcia (2010), Seismic imaging of staircase layers below the Mediterranean undercurrent, *Deep Sea Res. Part I: Oceanog. Res. Papers*, 57(10), 1345-1353, doi:10.1016/j.dsr.2010.07.001.

Bouzinac, C., J. Font, and C. Millot (1999), Hydrology and currents observed in the channel of Sardinia during the PRIMO-1 experiment from November 1993 to October 1994, *J. Mar. Sys.*, 20, 333-355, doi: 10.1016/S0924-7963(98)00074-8.

Boyd, J. D. and R. S. Linzell (1993), The temperature and depth accuracy of Sippican T-5 XBTs (No. NRL-JA-331-059-92), *Naval Oceanographic and Atmospheric Research Lab*, Stennis Space Center MS.

Budillon, G., G. P. Gasparini, and K. Schroeder (2009), Persistence of an eddy signature in the central Tyrrhenian basin, *Deep Sea Res. Part II*: Topical Studies in Oceanography, 56(11), 713-724, doi:10.1016/j.dsr2.2008.07.027.

875 Buffett, G. G., B. Biescas, J.L. Pelegrí, F. Machín, V. Sallarès, R. Carbonell, D. Klaeschen,
876 and R.W. Hobbs (2009), Seismic reflection along the path of the Mediterranean
877 Undercurrent, *Cont. Shelf Res.*, 29(15), 1848-1860, doi:10.1016/j.csr.2009.05.017.

878 Buffett, G. G., C. A. Hurich, E. A. Vsemirnova, R. W. Hobbs, V. Sallarès, R. Carbonell, D.
879 Klaeschen, and B. Biescas (2010), Stochastic Heterogeneity Mapping around a
880 Mediterranean salt lens, *Ocean Sci.*, 6, 423–428.

881 Buffett, G. G., J. L. Pelegrí, J. de la Puente, and R. Carbonell (2012), Real time visualization
882 of thermohaline finestructure using Seismic Offset Groups, *Meth. Oceanog.*, 3, 1-13,
883 doi:10.1016/j.mio.2012.07.003.

884 Cardin, V., G. Civitarese, D. Hainbucher, M. Bensi, and A. Rubino (2015), Thermohaline
885 properties in the Eastern Mediterranean in the last three decades: is the basin returning to the
886 pre-EMT situation?, *Ocean Sci.*, 11(53-66), 2015, doi: 10.5194/osd-11-391-2014.

887 Cohen, J. K. and J. W. Stockwell (2001), CWP/SU: Seismic Unix Release 35: a free package
888 for seismic research and processing, Center for wave phenomena, Colorado School of Mines.

889 Dagnino, D., V. Sallarès, B. Biescas, and C. R. Ranero (2016), Fine-scale thermohaline ocean
890 structure retrieved with 2-D prestack full-waveform inversion of multichannel seismic data:
891 Application to the Gulf of Cadiz (SW Iberia), *J. Geophys. Res. Oceans.*, 121, 5452–5469,
892 doi:10.1002/2016JC011844.

893 Davies, J. H., and D. R. Davies (2010), Earth's surface heat flux, *Solid Earth*, 1(1), 5.

894 Fer, I., P. Nandi, W. S. Holbrook, R. W. Schmitt, and P. Paramo (2010), Seismic imaging of
895 a thermohaline staircase in the western tropical North Atlantic, *Ocean Sci.*, 6(3), 621, doi:
896 10.5194/os-6-621-2010.

897 Fuda, J. -L., G. Etiope, C. Millot, P. Favali, M. Calcara, G. Smriglio, and E. Boschi (2002),
898 Warming, salting and origin of the Tyrrhenian Deep Water, *Geophys. Res. Lett.*, 29(19),
899 doi:10.1029/2001GL014072.

900 Garrett, C., and W. Munk (1975), Space-time scales of internal waves: A progress report, *J.*
901 *Geophys. Res.*, 80(3), 291-297, doi: 10.1029/JC080i003p00291.

902 Garrett, C., and W. Munk (1979), Internal waves in the ocean, *Annu. Rev. Fluid Mech.*, 11(1),
903 339-369, doi: 10.1146/annurev.fl.11.010179.002011.

904 Gonella, J., and D. Michon (1988), Deep internal waves measured by seismic-reflection
905 within the eastern Atlantic water mass, *C. R. Acad. Sci. Paris Ser. II*, 306(12), 781-787.

906 Hobbs, R. W., D. Klaeschen, V. Sallarès, E. Vsemirnova, and C. Papenberg (2009), Effect of
907 seismic source bandwidth on reflection sections to image water structure, *Geophys. Res. Lett.*,
908 36(24), doi:10.1029/2009GL040215.

909 Holbrook, W. S., P. Páramo, S. Pearse and R.W. Schmitt (2003), Thermohaline fine structure
910 in an oceanographic front from seismic reflection profiling, *Science*, 301(5634), 821-824,
911 doi: 10.1126/science.1085116.

912 Holbrook, W. S., and I. Fer (2005), Ocean internal wave spectra inferred from seismic
913 reflection transects, *Geophys. Res. Lett.*, 32(15), doi: 10.1029/2005GL023733.

914 Holbrook, W. S., I. Fer, R. W. Schmitt, D. Lizarralde, J. M. Klymak, L. C. Helfrich, R.
915 Kubichek (2013), Estimating oceanic turbulence dissipation from seismic images. *J. Atmos.*
916 *Oceanic Technol.*, 30, 1767-1788, doi:10.1175/JTECH-D-12-00140.1.

917 Hopkins, T. S. (1988), Recent observations on the intermediate and deep water circulation in
918 the Southern Tyrrhenian Sea, *Oceanolo. Acta*, special issue.

919 Iacono, R., E. Napolitano, S. Marullo, V. Artale, and A. Vetrano (2013), Seasonal variability
920 of the Tyrrhenian Sea surface geostrophic circulation as assessed by altimeter data, *J. Phys.*
921 *Oceanog.*, 43(8), 1710-1732, doi: 10.1175/JPO-D-12-0112.1.

922 Johannessen, O. M., and O. S. Lee (1974), A deep stepped thermohaline structure in the
923 Mediterranean, *Deep Sea Res. and Oceanog. Abstracts*, 21(8), 629-639.

924 Juza, M., L. Renault, S. Ruiz, and J. Tintoré (2013), Origin and pathways of Winter
925 Intermediate Water in the Northwestern Mediterranean Sea using observations and numerical
926 simulation, *J. Geophys. Res.: Oceans*, 118(12), 6621-6633, doi: 10.1002/2013JC009231.

927 Katz, E. J., and M. G. Briscoe (1979), Vertical coherence of the internal wave field from
928 towed sensors, *J. Phys. Oceanog.*, 9(3), 518-530, doi: 10.1175/1520-
929 0485(1979)009<0518:VCOTIW>2.0.CO;2.

930 Klaeschen, D., R. W. Hobbs, G. Krahmann, C. Papenberg, and E. Vsemirnova (2009),
931 Estimating movement of reflectors in the water column using seismic oceanography,
932 *Geophys. Res. Lett.*, 36(24), doi: 10.1029/2009GL038973.

933 Krahmann, G., P. Brandt, D. Klaeschen, and T. Reston (2008), Mid-depth internal wave
934 energy off the Iberian Peninsula estimated from seismic reflection data, *J. Geophys. Res.:*
935 *Oceans*, 113(C12), doi: 10.1029/2007JC004678.

936 Locarnini, R. A., A. V. Mishonov, J. I. Antonov, T. P. Boyer, H. E. Garcia, O. K. Baranova,
937 M. M. Zweng, C. R. Paver, J. R. Reagan, D. R. Johnson, M. Hamilton, and D. Seidov (2013),
938 *World Ocean Atlas 2013*, Volume 1: Temperature, S. Levitus, Ed., A. Mishonov Technical
939 Ed.; NOAA Atlas NESDIS 73, 40 pp.

940 Marani M. P., F. Gamberi and E. Bonatti (2004), From seafloor to deep mantle: architecture
941 of the Tyrrhenian backarc basin, *Mem. Descr. Carta Geol. D'It.*, 64 (LXIV).

942 MediMap Group (2005), Morpho-bathymetry of the Mediterranean Sea, *CIESM / Ifremer*
943 special publication, Atlases and maps, two maps at 1/2.000.

944 Ménesguen, C., B. L. Hua, X. Carton, F. Klingelhoefer, P. Schnürle, and C. Reichert (2012),
945 Arms winding around a meddy seen in seismic reflection data close to the Morocco coastline,
946 *Geophys. Res. Lett.*, 39, L05604, doi:10.1029/2011GL050798.

947 Millot, C. (1999), Circulation in the western Mediterranean Sea, *J. Mar. Sys.*, 20(1), 423-442,
948 doi: 10.1016/S0924-7963(98)00078-5.

949 NASA Earth Observations, AQUA/MODIS:
950 https://neo.sci.gsfc.nasa.gov/view.php?datasetId=MY1DMW_CHLORA&date=2010-04-01

951 Moeller, S., I. Grevemeyer, C. R. Ranero, C. Berndt, D. Klaeschen, V. Sallarès, N. Zitellini,
952 and R. Franco (2014), Crustal thinning in the northern Tyrrhenian Rift: Insights from
953 multichannel and wide-angle seismic data across the basin, *J. Geophys. Res.: Solid Earth*,
954 119(3), 1655-1677, doi: 10.1002/2013JB010431.

955 Papenberg, C., D. Klaeschen, G. Krahmann, and R. W. Hobbs (2010), Ocean temperature and
956 salinity inverted from combined hydrographic and seismic data, *Geophys. Res. Lett.*, 37(4),
957 doi: 10.1029/2009GL042115.

Piété, H., L. Marié, B. Marsset, Y. Thomas, and M. A. Gutscher (2013), Seismic reflection imaging of shallow oceanographic structures, *J. Geophys. Res.: Oceans*, 118(5), 2329-2344, doi: 10.1002/jgrc.20156.

Pinardi, N., M. Zavatarellia, M. Adanib, G. Coppini, C. Fratianni, P. Oddo, S. Simoncelli, M. Tonani, V. Lyubartsev, S. Dobricic, A. Bonaduced (2015), Mediterranean Sea large-scale low-frequency ocean variability and water mass formation rates from 1987 to 2007: A retrospective analysis, *Prog. Oceanog.*, 132, 318-332, doi: 10.1016/j.pocean.2013.11.003.

Poulain, P.-M., M. Menna, E. Mauri (2012), Surface geostrophic circulation of the Mediterranean Sea derived from drifter and satellite altimeter data, *J. Phys. Oceanog.*, 42, 973-990, doi: 10.1175/JPO-D-11-0159.1.

Prada, M., V. Sallarès, C. R. Ranero, M. G. Vendrell, I. Grevemeyer, N. Zitellini, and R. de Franco (2014), Seismic structure of the Central Tyrrhenian basin: geophysical constraints on the nature of the main crustal domains, *J. Geophys. Res.: Solid Earth*, 119(1), 52-70, doi: 10.1002/2013JB010527.

Prada, M., V. Sallarès, C. R. Ranero, M. G. Vendrell, I. Grevemeyer, N. Zitellini, R. de Franco (2015), The complex 3-D transition from continental crust to backarc magmatism and exhumed mantle in the Central Tyrrhenian basin, *Geophys. J. Int.*, 203(1), 63-78, doi: 10.1093/gji/ggv271.

Prada, M., V. Sallares, C. R. Ranero, M. G., Vendrell, I. Grevemeyer, N. Zitellini, & R. Franco, (2016). Spatial variations of magmatic crustal accretion during the opening of the Tyrrhenian back-arc from wide-angle seismic velocity models and seismic reflection images. *Basin Res.* doi:10.1111/bre.12211.

Quentel, E., X. Carton, M.-A. Gutscher, and R. Hobbs (2010), Detecting and characterizing mesoscale and submesoscale structures of Mediterranean water from joint seismic and hydrographic measurements in the Gulf of Cadiz, *Geophys. Res. Lett.*, 37, L06604, doi:10.1029/2010GL042766.

Radko, T. (2005), What determines the thickness of layers in a thermohaline staircase? *J. Fluid Mech.*, 523, 79-98, doi: 10.1017/S0022112004002290.

Ranero, C. R. and the MEDOC team. "El MEDeterráneo OCcidental (MEDOC), The Western Mediterranean basins: a natural laboratory to study the processes of formation of rifted continental margins." (2010).

Ravens, J. (1995), Globe Claritas Seismic Processing Manual, Institute of Geological and Nuclear Sciences.

Rinaldi, E., B. Buongiorno Nardelli, E. Zambianchi, R. Santoleri, and P. -M. Poulain (2010), Lagrangian and Eulerian observations of the surface circulation in the Tyrrhenian Sea, *J. Geophys. Res.: Oceans*, 115(C4), doi: 10.1029/2009JC005535.

Ruddick, B., H. Song, C. Dong, and L. Pinheiro (2009), Water column seismic images as maps of temperature gradient, *Oceanog.*, 22(1), 192, doi: 10.5670/oceanog.2009.19.

Ruddick, B., and A. E. Gargett (2003), Oceanic double-diffusion: introduction, *Prog. Oceanog.* 56 (2003) 381–393, doi:10.1016/S0079-6611(03)00024-7.

Sallarès, V., B. Biescas, G. G. Buffett, R. Carbonell, J. J. Dañobeitia, and J. L. Pelegrí (2009), Relative contribution of temperature and salinity to ocean acoustic reflectivity, *Geophys. Res. Lett.*, 36(24), doi: 10.1029/2009GL040187.

Sallarès, V., J. F. Mojica, B. Biescas, D. Klaeschen, and E. Gràcia (2016), Characterization of the sub-mesoscale energy cascade in the Alboran Sea thermocline from spectral analysis of high-resolution MCS data, *Geophys. Res. Lett.*, doi: 10.1002/2016GL069782.

Schlitzer, R., Ocean Data View, http://odv.awi.de, (2013).

Schmitt, R. W., H. Perkins, J. D. Boyd, and M. C. Stalcup (1987), C-SALT: An investigation of the thermohaline staircase in the western tropical North Atlantic, *Deep Sea Res. Part A, Oceanog. Res. Papers*, 34(10), 1655-1665, doi: 10.1016/0198-0149(87)90014-8.

Schmitt, R. W. (1994), Double diffusion in oceanography, *Annu. Rev. Fluid Mech.*, 26(1), 255-285.

Schmitt, R. W., J. R. Ledwell, E.T. Montgomery, K. L. Polzin, and J. M. Toole (2005), Enhanced Diapycnal Mixing by Salt Fingers in the Thermocline of the Tropical Atlantic, *Science*, 308(5722), 685-688.

1013 Sparnocchia, S., G. P. Gasparini, M. Astraldi, M. Borghini, and P. Pistek (1999), Dynamics
1014 and mixing of the Eastern Mediterranean outflow in the Tyrrhenian basin, *J. Mar. Sys.*, 20(1),
1015 301-317, doi: 10.1016/S0924-7963(98)00088-8.

1016 Stern, M. E. (1960), The 'salt-fountain' and thermohaline convection, *Tellus*, 12, 172-175.

1017 Tait, R. I., and M. R. Howe (1971), Thermohaline staircase, *Nature*, 231, 178-179, doi:
1018 10.1038/231178a0.

1019 Testor P., Béranger K., and L. Mortier, 2005, Modeling the deep eddy field in the
1020 southwestern Mediterranean: the life cycle of Sardinian Eddies, *Geophys. Res. Lett.*, 32, No.
1021 13, L13602, doi:10.1029/2004GL022283.

1022 Thomsen, S., T. Kanzow, G. Krahmann, R. J. Greatbatch, M. Dengler, and G. Lavik (2016),
1023 The formation of a subsurface anticyclonic eddy in the Peru-Chile Undercurrent and its
1024 impact on the near-coastal salinity, oxygen, and nutrient distributions, *J. Geophys. Res.:*
1025 *Oceans*, 121(1), 476-501, doi: 10.1002/2015JC010878.

1026 Thorpe, S. A. (1975), The excitation, dissipation, and interaction of internal waves in the
1027 deep ocean, *J. Geophys. Res.*, 80(3), 328-338, doi: 10.1029/JC080i003p00328.

1028 Viúdez, Á., and J. Tintoré (1995), Time and space variability in the eastern Alboran Sea from
1029 March to May 1990, *J. Geophys. Res.: Oceans*, 100(C5), 8571-8586, doi:
1030 10.1029/94JC03129.

1031 Viúdez, A., J. M. Pinot, and R. L. Haney (1998), On the upper layer circulation in the
1032 Alboran Sea, *J. Geophys. Res.: Oceans*, 103(C10), 21653-21666, doi: 10.1029/98JC01082.

1033 Wessel, P., and W. H. Smith (1998), New, improved version of Generic Mapping Tools
1034 released, *Eos*, Transactions American Geophysical Union, 79(47), 579-579, doi:
1035 10.1029/98EO00426.

1036 Williams, A. J. (1975), Images of ocean microstructure. *Deep Sea Res.* 22(12), 811-829.

1037 Yilmaz, Ö. (2001). Seismic data analysis (Vol. 1). *Soc. Expl. Geophys.*

Zodiatis, G., and G. P. Gasparini (1996), Thermohaline staircase formations in the Tyrrhenian Sea, *Deep Sea Res. Part I: Oceanog. Res. Papers*, 43(5), 655-678, doi: 10.1016/0967-0637(96)00032-5.

Zweng, M. M, J. R. Reagan, J. I. Antonov, R. A. Locarnini, A. V. Mishonov, T. P. Boyer, H. E. Garcia, O. K. Baranova, D. R. Johnson, D. Seidov, M. M. Biddle (2013), *World Ocean Atlas 2013*, Volume 2: Salinity, S. Levitus, Ed., A. Mishonov Technical Ed.; NOAA Atlas NESDIS 74, 39 pp. 2013.

1061

1062

1063

1064

1065 **Supplementary Material**

1066

1067 Appendix 1 – Acquisition and processing parameters

Energy source (Sercel® GGUN-II)	
Total volume	49.8 L (3040 cu.in)
Nominal source depth	10 m
Nominal shot point interval	50 m
Dominant frequency	60 Hz
Instrumentation (Eiva® software)	
Format	SEG-D
Sample rate	2 ms
Record length	18 s
Band-pass filter	OUT—90/100 Hz
Cable configuration	
Streamer length	3450 m
Number of channel groups	276
Group interval	12.5 m
Nominal cable depth	15 m

Near offset	120 m
Common mid-point spacing	6.25 m

Seismic data acquisition parameters

Acquisition zone	Start Time/Date	End Time/Date	Start N Lat	Start E Long	End N Lat	End E Long
Seismic section EF	19:55 27 April 2010	07:13 29 April 2010	40.50°	10.00°	40.50°	13.80°
Seismic section IJ	21:30 01 May 2010	04:32 03 May 2010	40.30°	9.79°	40.30°	13.21°
Seismic section GH	21:41 29 April 2010	17:10 01 May 2010	40.00°	14.41°	40.00°	9.80°
XBT segment EF-1	01:39 28 April 2010	08:36 28 April 2010	40.50°	10.74°	40.50°	11.52°
XBT segment EF-2	17:36 28 April 2010	01:36 29 April 2010	40.50°	12.37°	40.50°	13.18°
XBT segment IJ-1	05:10 02 May 2010	12:38 02 May 2010	40.30°	10.59°	40.30°	11.35°
XBT segment IJ-2	20:45 02 May 2010	03:30 03 May 2010	40.30°	12.36°	40.30°	13.11°
XBT segment GH-1	01:24 01 May 2010	09:24 01 May 2010	40.00°	11.51°	40.00°	10.70°
XBT segment GH-2	09:15 30 April 2010	17:15 30 April 2010	40.00°	13.24°	40.00°	12.38°
CTD for section EF	04:05 14 April 2010	N/A	40.50°	12.18°	N/A	N/A
CTD for section IJ	23:07 13 April 2010	N/A	40.25°	12.61°	N/A	N/A
CTD for section GH	04:57 13 April 2010	N/A	40.00°	12.40°	N/A	N/A
Glider (outbound)	15:08 22 April 2010	11:56 27 April 2010	40.50°	13.24°	40.50°	12.38°
Glider (inbound)	11:56 27 April 2010	23:45 02 May 2010	40.50°	12.38°	40.50°	13.24°

Data acquisition times and locations.

Appendix 2 – Seismic data processing

Digital seismic data processing is a series of mathematical operations that manipulate seismic traces (time series) to image the subsurface (see Yilmaz, 2001 for a complete discussion). For the datasets used in this study, we first designed a back projection algorithm to arrive at an optimal geometry configuration. This accounted for small deviations in the streamer's position due to forcing by surface currents (so-called 'feathering'). This was done by tracking along near-offset streamer positions, which are at a comparatively fixed lateral offset from the GPS-determined shot point positions. In contrast, the recording channels near the end of the streamer may be laterally offset by tens-to-hundreds of meters. Next, we applied a bulk shift of -64 ms to correct for a recording time delay that results from the source and receiver being towed at a depth of a few meters. We then applied a high-pass band pass filter at 3 Hz (with a taper of 18 dB/octave) to remove low-frequency swell noise. One effect of the band pass filter is to limit the effective resolution of the data set. Our filter gave a dominant frequency of 60 Hz, which corresponds to a dominant wavelength of about 25 m. In studies of the solid earth, the Rayleigh criterion is often used to deduce the maximum vertical resolution as one-quarter of the dominant wavelength. However, unlike rocks, heat and mass diffusion across water mass boundaries produces a gradual change in acoustic impedance [Hobbs et al., 2009]. So, we conservatively put our maximum vertical resolution at 10 m. The effective horizontal resolution is determined by the common-midpoint (CMP) spacing, which was 6.25 m.

To attenuate the direct wave noise (the acoustic wave which travels directly between source and receiver without reflecting — along the streamer cable), we applied a linear moveout correction using an optimal sound speed of 1509 m/s that was determined empirically by ensuring that the direct wave was horizontally aligned. Next, we applied a trace mix with a

weighting across 69 traces followed by adaptive subtraction of the direct wave energy. Finally, the linear moveout correction was restored.

We used a multichannel dip filter with removable automatic gain control (AGC) to reject energy with negative dips in order to minimize the strongest wrap-around multiple noise. Next, we applied a normal moveout correction (NMO) using a location-dependent sound speed function derived from co-located XBT temperature data. Salinity information for this calculation was obtained from a depth-dependent temperature-salinity relationship that was derived from nearby CTD data [Papenberg et al., 2010] — a valid approach in cases when at most two water masses are present at any depth so that a non-ambiguous linear relationship between salinity and temperature can be derived. We then used two different dip filter designs to remove energy outside the maximum expected reflector dip in the sections. A linear radon velocity filter with a maximum dip of +/- 300 ms at 3600 m offset, as well as a radial prediction filter with a correlation length of five traces and a scan width of +/- 5 ms improved trace-to-trace signal coherency in the shot gather. A final band-pass filter of 5–90 Hz with high-pass and low-pass tapered slopes of 18 and 57 dB/octave, respectively, completed the pre-processing.

We sorted the data by CMP location, stacked them, applied an amplitude preserving post-stack Kirchhoff time migration, and converted two-way time (vertical axis) to depth using an average sound speed of 1509 m/s. Lastly, for display we applied a post-stack running trace mix to improve lateral coherency by removing random noise.

Appendix 3 – Chlorophyll satellite data

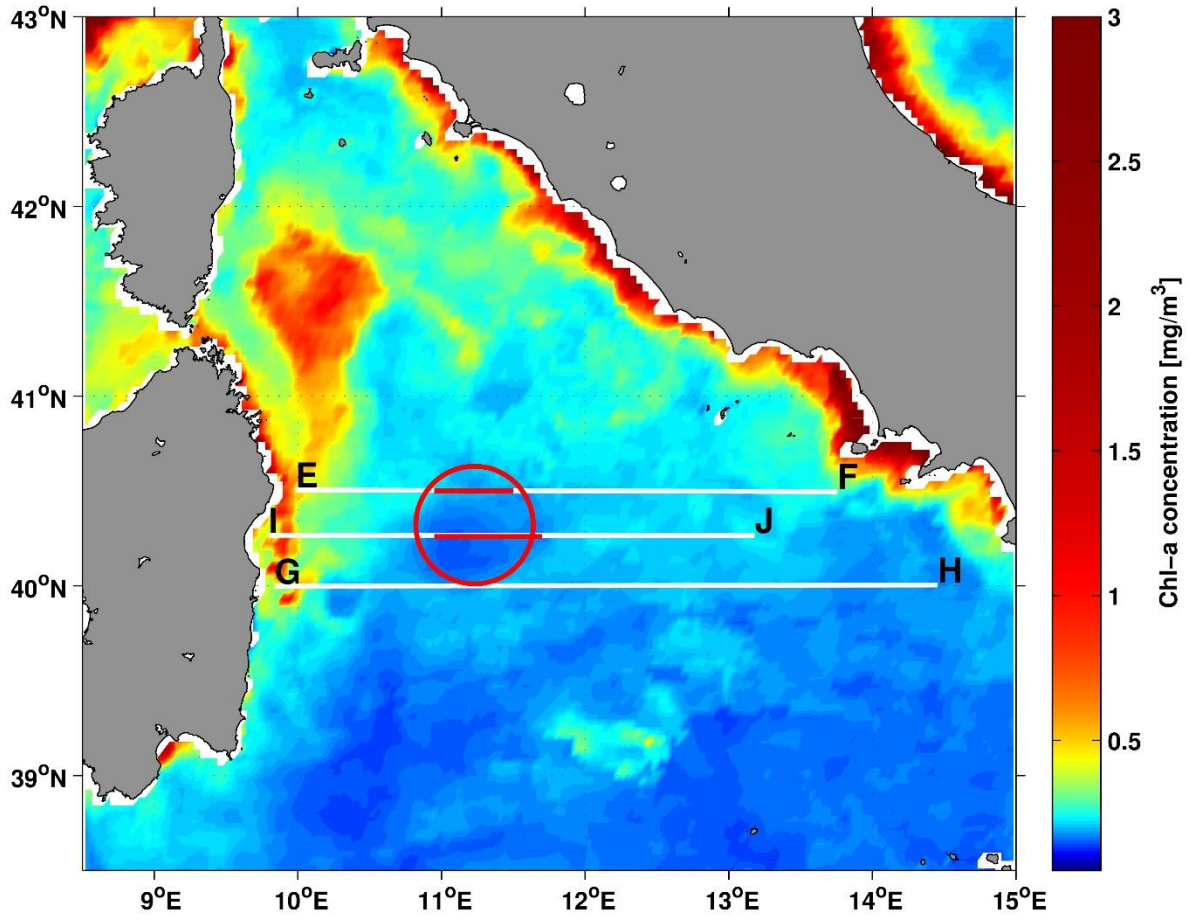

Location of seismic sections (white lines and black labels) superimposed over chlorophyll concentrations from AQUA/MODIS satellite observations (http://neo.sci.gsfc.nasa.gov). The chlorophyll satellite data was obtained as an average over a period of 40 days centered at the time of the seismic sections. The estimated location of the eddy is indicated by the red circle. The red segments in the inset of Figure 1 indicate the location where the seismic reflection data clearly show the eddy.

Appendix 4 – Calculated average energy levels

	Section EF	Section IJ	Section GH
Eddy	0.65±0.04	0.78±0.06	(0.98±0.07)
Western end of section	1.51±0.07	1.48±0.07	1.34±0.06
Staircase area	0.45±0.02	0.47±0.02	0.46±0.02
All	1.09±0.05	1.12±0.06	1.06±0.04
Garrett-Munk model	2.5	2.5	2.5

Average energy levels ($m^2 \cdot h^{-1}$) of selected parts of the sections and of the whole sections. Note that section GH did not clearly show the bowl-shaped reflectors of the eddy. Nevertheless, the respective part of the section showed slightly decreased energy levels, so we include the value in parenthesis. To put the energy values into context we also show the energy level expected from the Garrett and Munk model for a buoyancy frequency of 2.0 cph at the latitude of the Tyrrhenian Sea.

Appendix 5 – high resolution seismic sections

High resolution seismic sections of Figure 2 are available as a PDF file in A3 format.

1167

1168

1169

1170 Figure Captions

1171 Figure 1 - Circulation in the Tyrrhenian Sea (modified after Millot [1999]) superimposed on
1172 multibeam bathymetry (MediMap Group [2005]) — depth color scale given in meters at
1173 right. Path of Atlantic Water (AW) shown in white; Levantine Intermediate Water (LIW)
1174 shown in red; Tyrrhenian Dense Water (TDW) shown in yellow; Western Mediterranean
1175 Deep Water (WMDW) shown in green. Selected seafloor features are 1: Secchi Seamount; 2:
1176 Farfalla Seamount; 3: Caesar Seamount; 4: Magnaghi Volcano; 5: Vavilov Seamount; 6:
1177 Flavio Gioia Seamount, [Mariani et al., 2004]. *Inset*: locations of seismic sections are shown
1178 in light blue; XBT deployment segments are indicated in orange; autonomous glider
1179 deployment shown in dotted yellow; eddy-dominated locations (Figure 3) are indicated by
1180 white segments; staircase-dominated regions (Figures 4, 5 and 6) are indicated by yellow
1181 segments; CTD locations are shown as red circles.

1182

1183 Figure 2: Full seismic sections displayed in true relative sizes. From top to bottom, section
1184 EF, IJ and GH. Blue boxes indicate the position of XBT deployments. Yellow box shows the
1185 location of the autonomous glider deployment. Red vertical lines indicate positions of CTD
1186 profiles shown on the left side of each seismic section. Sea floor features are indicated.
1187 Appendix 5 contains the seismic images in high-resolution A3 PDF format to view or print.

1188

1189 Figure 3 – a) a portion of seismic section EF showing a near surface eddy, b) part of seismic
1190 section IJ showing the same eddy, and a smaller eddy to the west. Shown in black and white
1191 shading are the seismic reflection data and in color the XBT temperature observations.
1192 Spatial scales and longitude coordinates are indicated. Lateral extents of eddies shown in this
1193 figure are depicted as white segments in the inset of Figure 1.

Figure 4 – Tyrrhenian Sea thermohaline staircases for XBT segment EF-2 and the nearest CTD profile (left) showing a correlation with the thermohaline staircase steps. Red line indicates corresponding longitude of CTD; for its precise location refer to Appendix 1. Shown in black and white shading are the seismic reflection data and in color the XBT temperature observations. Spatial scales and longitude coordinates are indicated. See also Figure 1.

Figure 5 – Tyrrhenian Sea thermohaline staircases for XBT zone IJ-2 and the nearest CTD profile (left) showing a correlation with the thermohaline staircase steps. Red line indicates corresponding longitude of CTD; for its precise location refer to Appendix 1. Shown in black and white shading are the seismic reflection data and in color the XBT temperature observations. Spatial scales and longitude coordinates are indicated. See also Figure 1.

Figure 6 – Tyrrhenian Sea thermohaline staircases for XBT zone GH-2 and the nearest CTD profile (left) showing a correlation with the thermohaline staircase steps. Red line indicates corresponding longitude of CTD; for its precise location refer to Appendix 1. Shown in black and white shading are the seismic reflection data and in color the XBT temperature observations. Spatial scales and longitude coordinates are indicated. See also Figure 1.

Figure 7 – Salinity data from autonomous glider mapped over greyscale seismic data. Top panel is outbound measurement. Bottom panel is inbound measurement. See Figures 1 and 2 and Appendix 1 for location.

Figure 8: Smoothed buoyancy frequency profiles calculated from R/V Urania CTD data and from WOA13 climatological data [Locarnini et al., 2013; Zweng et al., 2013]. The blue profile was used to normalize the energy density spectra of vertical excursions of the reflectors.

Figure 9: Average horizontal wave number spectra of normalized internal wave energy density for the three sections. Also shown is the internal wave spectrum expected for open

1224 ocean conditions, black line [Garrett and Munk, 1975, Katz and Briscoe, 1979] for the
1225 latitude range of the three sections and for a buoyancy frequency of 2.0 cph. The gray area
1226 marks the interval over which the spectra were integrated for the energy level comparisons.

1227

1228 Figure 10: Internal wave energy levels ($m^2 \cdot h^{-1}$) averaged over 100 m thick depth intervals and
1229 1000 CDP (6.25 km) wide horizontal intervals mapped over grayscale seismic data. The
1230 energy levels show distinct regional differences that appear to coincide with features found in
1231 the seismic reflection data. The three boxes in each panel show areas (blue: Sardinia shelf
1232 break region, red: eddy region, green: staircase region) over which the averages from
1233 Appendix 4 were calculated.

1234

1235 Figure 11: Average normalized internal wave energy levels of the three sections plotted
1236 against depth showing a distinct vertical variation.

1237

1238